Astronomy & Astrophysics

The near-infrared spectral energy distribution of β Pictoris b[★,★★]

M. Bonnefoy[1], A. Boccaletti[2], A.-M. Lagrange[3], F. Allard[4], C. Mordasini[1], H. Beust[3], G. Chauvin[3], J. H. V. Girard[5], D. Homeier[4], D. Apai[6,7], S. Lacour[2], and D. Rouan[2]

[1] Max Planck Institute for Astronomy, Königstuhl 17, 69117 Heidelberg, Germany
e-mail: bonnefoy@mpia-hd.mpg.de
[2] LESIA, Observatoire de Paris, CNRS, University Pierre et Marie Curie Paris 6 and University Denis Diderot Paris 7,
5 place Jules Janssen, 92195 Meudon, France
[3] UJF-Grenoble 1/CNRS-INSU, Institut de Planétologie et d'Astrophysique de Grenoble (IPAG) UMR 5274, 38041 Grenoble, France
[4] CRAL, UMR 5574, CNRS, Université de Lyon, École Normale Supérieure de Lyon, 46 allée d'Italie, 69364 Lyon Cedex 07, France
[5] European Southern Observatory, Casilla 19001, Santiago 19, Chile
[6] Department of Astronomy, 933 N. Cherry Avenue, Tucson, AZ 85721, USA
[7] Department of Planetary Sciences, The University of Arizona, 1929 E. University Blvd., Tucson, AZ 85721, USA

Received 3 December 2012 / Accepted 5 February 2013

ABSTRACT

Context. A gas giant planet has previously been directly seen orbiting at 8–10 AU within the debris disk of the ~12 Myr old star β Pictoris. The β Pictoris system offers the rare opportunity of both studying the physical and atmospheric properties of an exoplanet placed on a wide orbit and establishing its formation scenario.

Aims. We aim to build the 1–5 μm spectral energy distribution of the planet for the first time. Our goal is to provide secure and accurate constraints on its physical and chemical properties.

Methods. We obtained J (1.265 μm), H (1.66 μm), and M′ (4.78 μm) band angular differential imaging of the system between 2011 and 2012. We used Markov chain Monte Carlo simulations of the astrometric data to revise constraints on the orbital parameters of the planet. Photometric measurements were compared to those of ultra-cool dwarfs and young companions. They were combined with existing photometry (2.18, 3.80, and 4.05 μm) and compared to predictions from 7 PHOENIX-based atmospheric models in order to derive the atmospheric parameters ($T_{\rm eff}$, log g) of β Pictoris b. Predicted properties from ("hot-start", "cold-start", and "warm start") evolutionary models were compared to independent constraints on the mass of β Pictoris b. We used planet-population synthesis models following the core-accretion paradigm to discuss the planet's possible origin.

Results. We detect the planetary companion in our four-epoch observations. We estimate $J = 14.0 \pm 0.3$, $H = 13.5 \pm 0.2$, and $M' = 11.0 \pm 0.3$ mag. Our new astrometry consolidates previous semi-major axis (8–10 AU) and excentricity ($e \leq 0.15$) estimates of the planet. The location of β Pictoris b in color–magnitude diagrams suggests it has spectroscopic properties similar to L0-L4 dwarfs. This enables one to derive $\mathrm{Log}_{10}\,(L/L_{\odot}) = -3.87 \pm 0.08$ for the companion. The analysis with atmospheric models reveals that the planet has a dusty atmosphere with $T_{\rm eff} = 1700 \pm 100$ K and log $g = 4.0 \pm 0.5$. "Hot-start" evolutionary models give a new mass of 10^{+3}_{-2} $M_{\rm Jup}$ from $T_{\rm eff}$ and 9^{+3}_{-2} $M_{\rm Jup}$ from luminosity. Predictions of "cold-start" models are still inconsistent with independent constraints on the planet mass. "Warm-start" models constrain the mass to $M \geq 6$ $M_{\rm Jup}$ and the initial entropies to values ($S_{\rm init} \geq 9.3 K_{\rm b}$/baryon) midway between those considered for cold/hot-start models, but probably closer to those of hot-start models.

Key words. instrumentation: adaptive optics – techniques: photometric – planetary systems – stars: individual: β Pic b – planets and satellites: atmospheres – planets and satellites: fundamental parameters

1. Introduction

Understanding planetary systems's formation and evolution has become one of the outstanding topics in astronomy, ever since the imaging of a debris disk around the young (≃12 Myr) and massive star ($M = 1.75\ M_{\odot}$) β Pictoris, in the 80s (Smith & Terrile 1984) and the discovery of the first exoplanet around a solar-type star in the 90s (Mayor & Queloz 1995). The few dozen wide-orbit (>5 AU) planetary mass companions directly imaged around young and nearby stars suggest that alternative formation mechanisms to the core-accretion scheme preferred for closer-in exoplanets should be considered. In particular, the four giants planets discovered at projected separations of 15–68 AU around

the young and massive star HR 8799 (Marois et al. 2008, 2010b) can not all be explained by in-situ formation by core accretion. Instead, disk instability has been proposed to account for the observed properties of these objects (Dodson-Robinson et al. 2009; Boss 2011).

The atmospheric properties of wide-orbit (nonirradiated) and young (≲150 Myr old) "exoplanets" discovered by direct imaging can be studied based on multiple-band photometry (Chauvin et al. 2004b) and even low-resolution spectra (Vigan et al. 2008) in the near-infrared (1–5 μm). Barman et al. (2011b) and Skemer et al. (2011) have used atmospheric models to conclude that the nonequilibrium chemistry of CO/CH_4 and/or thick clouds of refractory elements could account for the photometric and spectroscopic properties of the planetary mass companion 2M1207b. Bonnefoy et al. (2010) and Faherty et al. (2013) have also recently shown that the near-infrared (1.1−1.4 μm and 1.5−2.5 μm) spectra of young planetary mass companions AB Pic b and 2M1207 b match those of young and isolated

---

Table 1. Log for the new *J*, *H*, and *M′*-band observations.

Date	Band	Density filter	Camera	DIT (s)	NDIT	N_{exp}	$\theta_{start}{}^a$ (°)	$\theta_{end}{}^b$ (°)	EC mean^c (%)	τ_0 mean^d (ms)
16/12/2011	*J*	ND_short	S13	0.500	100	8	−34.110	−30.882	60.95	3.26
16/12/2011	*J*	...	S13	0.500	100	48	−25.394	−2.596	61.11	3.87
16/12/2011	*J*	ND_short	S13	0.500	100	8	−2.309	1.514	59.60	3.73
18/12/2011	*H*	ND_short	S13	0.500	100	8	−28.267	−24.834	56.86	2.79
18/12/2011	*H*	...	S13	0.500	100	48	−24.559	−1.654	54.17	2.52
18/12/2011	*H*	ND_short	S13	0.500	100	8	−1.350	2.525	56.61	2.21
11/01/2012	*H*	ND_short	S13	0.200	150	8	−26.530	−24.305	56.60	3.42
11/01/2012	*H*	...	S13	0.400	150	84	−22.563	12.082	61.00	3.18
11/01/2012	*H*	ND_short	S13	0.200	150	8	14.879	17.268	71.55	2.80
26/11/2012	*M′*	ND_long	L27	0.100	250	8	−28.362	−26.063	27.93	1.27
26/11/2012	*M′*	...	L27	0.065	300	184	−19.482	32.322	19.72	1.10
26/11/2012	*M′*	ND_long	L27	0.130	150	8	32.721	34.411	13.25	0.96

Notes. $^{(a)}$ Parallactic angles (θ) at the begining of the observations. $^{(b)}$ Parallactic angles (θ) at the end of the observations. $^{(c)}$ Average coherent energy during the observations. $^{(d)}$ Average coherence time during the observations.

brown dwarfs (Kirkpatrick et al. 2006; Cruz et al. 2009). This also provided the empirical evidence that some of the peculiar photometric/spectroscopic features of these companions can be interpreted as a consequence of their lower surface gravity (compared to field L-T dwarfs). The description of the photometric and spectroscopic properties of the cooler planets found around HR 8799 requiere a more complex picture possibly involving thick clouds (Madhusudhan et al. 2011; Currie et al. 2011a), nonequilibrium chemistry (Janson et al. 2010; Barman et al. 2011a) or even multiple cloud layers Skemer et al. (2012). It is still unclear whether these properties account for the young age – and reduced surface gravity – of the objects (Marley et al. 2012) or could be related to the peculiar nature of this system.

The star β Pictoris is one of the best laboratories for the study of early phasis of planetary systems formation and evolution. It has been the subject of hundreds of observations over a broad spectral range. With NaCo at VLT, we detected a giant planet orbiting the star (Lagrange et al. 2009, 2010), roughly along the dust disk position angle (PA), with a semi-major axis *a* between 8 and 14 AU. Its observed *L′* luminosity (3.8 μm) indicated it has $T_{eff} \simeq 1700$ K and a mass of 7–11 M_{Jup}. Follow-up observations at 4.05 μm (NB_4.05 filter; Quanz et al. 2010) and at 2.18 μm (K_s band) (Bonnefoy et al. 2011) confirmed these values. Additional astrometric data obtained from October 2010 to March 2011 showed that the semi-major axis is in the range 8−10 AU, and the eccentricity is less than 0.2 (Fig. 1 of Chauvin et al. 2012). β Pictoris b is so far the closest planet ever imaged around a star.

These predictions of β Pictoris b properties (T_{eff}, mass), like those of imaged planets or companions rely, however, on models that are currently debated: either the so-called "hot-start" models that assume spherical collapse from an arbitrary large initial radius (Chabrier et al. 2000; Baraffe et al. 2003) or "cold-start" models (Marley et al. 2007; Spiegel & Burrows 2012; Mordasini et al. 2012), which are supposed to predict the properties of planets produced by accretion of gas through a super-critical accretion shock onto the planet embryo. "Cold-start" models of Marley et al. (2007) and Spiegel & Burrows (2012) predict giant planets more than 100 times fainter at 10 Myr than the "hot start" model. The main difference is due to the gas initial properties (temperature, entropy), which depends on the fate of the energy released during the gas accretion and shock process.

Based on current model predictions (Kennedy & Kenyon 2008) and given its separation, β Pictoris b could have formed
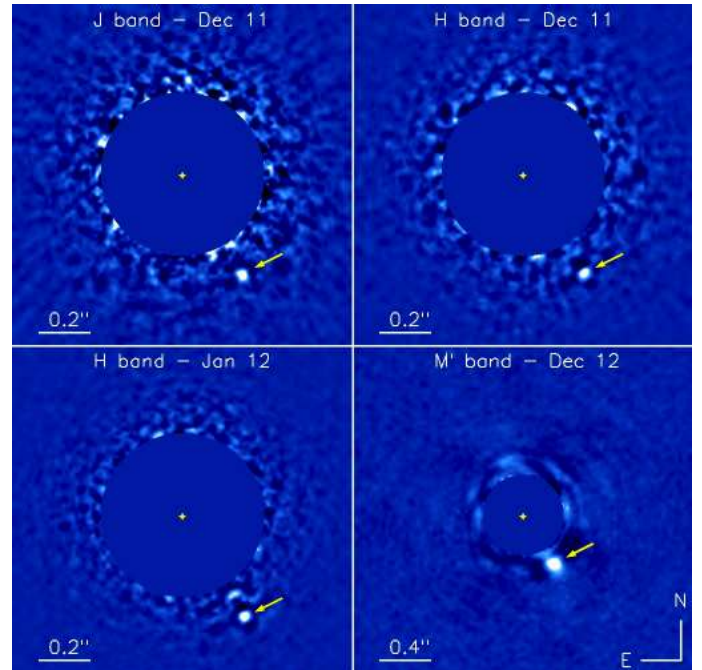

Fig. 1. Redetection of β Pictoris b in the *J* (*upper-left panel*) band, in the first (*upper-right panel*) and second epochs (*lower-left panel*) *H* band observations, and in the *M′* band (*lower-right panel*). Arrows indicate the planet position.

via core accretion (Lagrange et al. 2010). Using limits coming from radial velocities measurements (Lagrange et al. 2012a), we could constrain its dynamical mass to be ≤15.5 M_{Jup} and ≤12 M_{Jup} if the semi-major axis is shorter than 10 and 9 AU, respectively. Current "cold-start" models fail to predict masses from the available photometry that respect these dynamical mass constraints.

We present new data obtained at *J* (1.265 μm), *H* (1.66 μm), and *M′* (4.78 μm) bands that we combine to previously published data at 2.18, 3.8, and 4.05 μm to build the near-infrared (1–5 μm) spectral energy distribution (SED) of the planet. The goal of the study is to better characterize of the atmospheric (T_{eff}, log g, composition) and physical (radii, mass) properties of the companion needed to understand its formation process and evolution. The paper is organized as follows. Sections 2 and 3

describe the data and their processing, respectively. Our core results are presented in Sect. 4, divided in four main sections. In Sect. 4.1 we compare the resulting colors to those of reference young and old objects, found isolated or as companions to star/brown-dwarfs. We analyze in Sect. 4.2 the SED of the planet with atmospheric models. We present new orbital derived from new astrometry of the planet in Sect. 4.3. We derive new model-dependent mass estimates of the companion in Sect. 4.4. The results and their implications for the formation history of the planet are discussed in Sect. 5.

2. Observations

We used the Nasmyth Adaptive Optics System (NAOS) coupled to the Near-Infrared Imager and Spectrograph (CONICA) at VLT/UT4 (NACO; Lenzen et al. 2003; Rousset et al. 2003) to obtain four new high-contrast observations of β Pictoris (see Table 1) between December 2011 and November 2012.

The star was first observed on December 16, 2011 in the J band ($\lambda_c = 1.265\,\mu$m; width $= 0.25\,\mu$m) with the S13 camera. We consecutively recorded 4800×0.5 s exposures stored in 48 datacubes (100 frames each) in pupil-stabilized mode. The field orientation changed by $22.8°$ during this sequence. The data integration time was chosen to saturate the core of the flux distribution of β Pictoris over a radius of $\sim$150 mas. This and the choice of the appropriate reading mode (double_rd_rstd) ensured we had the necessary detector dynamics to detect the companion. The star was dithered ($\pm 3''$ amplitude) through the instrument field-of-view every 200 exposures (1 s) during the observations to perform a first-order subtraction of bad pixels, detector bias, and background. We took eigtht additional 100×0.5 s unsaturated exposures of the star with a neutral density (ND_short) before and after the sequence of saturated images. These data were later used for the calibration of the flux and position of β Pictoris b.

We repeated this sequence with the H band filter ($\lambda_c = 1.66\,\mu$m; width $= 0.33\,\mu$m) on December 18, 2011. The parallactic angle variation is close to the one of the J band sequence ($22.9°$ variation in field orientation).

We obtained second-epoch observations of β Pictoris in the H band on January 11, 2012. These observations benefited from excellent atmospheric conditions and increased field rotation ($34.6°$). We lowered the exposure time to 0.4s to maintain the saturated area to separations shorter than 70 mas. The star was kept at a fixed position in the instrument field of view (no dithering). We recorded a series of sky frames at the end of the sequence to subtract the bias and remove hot pixels. The suppression of telescope offsets and point-spread-function (PSF) drifts previously observed when tracking the pupil through meridian (see the NaCo user manual version 91.0) improve the stability of the PSF and simplify the registration of individual frames (see Sect. 3). Two sequences of $8 \times 150 \times 0.2$ s unstaturated exposures of the star were taken at the begining and end of the sequence for estimating the photometry and the astrometry.

We finally collected a sequence of M' band ($\lambda_c = 4.78\,\mu$m; width $=0.59\,\mu$m) saturated exposures (184 datacubes with 300 frames each and 0.065s individual integration times) of the star on November 26, 2012 in pupil-stabilized mode. The L27 camera ($\sim$27.12 mas/pixel) was used for these observations. We recorded eigtht unsaturated exposures with a neutral density (ND_long) before and after the sequence with a higher integration time (0.1 and 0.13 s, respectively) for the same purpose as above. The median observing conditions were degraded compared to the J and H band observations. Nevertheless, the

observations benefited from the improved Strehl ratio and PSF stability at these wavelengths.

3. Data processing

3.1. Initial steps

Each dataset is composed of a sequence of raw datacubes containing 100 to 300 frames each (see Table 1). We reduced the data using two independent pipelines (Lagrange et al. 2010, 2012a; Bonnefoy et al. 2011; Boccaletti et al. 2012; Chauvin et al. 2012; Milli et al. 2012). Pipelines first apply basic cosmetic steps to all the frames (sky subtraction, flat fielding, bad pixel interpolation) contained in each raw cubes. They use weighted bidimensional Moffat fitting to find the position of the saturated star for each exposure and center it on the field of view. The parallactic and hour angles associated to each frame is computed using the Universal Time corresponding to the first and last exposures contained in each raw cube[1]. Frames with low encircled energy and small saturated area are flagged and removed from the datacube. The datacubes are then binned temporally and placed in a final master cube. The master cube and the list of parallactic angles are used as input for routines that apply the classical-ADI (CADI; also often called "median-ADI"), radial-ADI (RADI; Marois et al. 2006), and LOCI (Lafrenière et al. 2007) algorithms to remove the flux distribution of the star. We also checked our results for three of the most favorable datasets (see Table 1) with the innovative algorithm of Soummer et al. (2012) based on principal component analysis (KLIP).

3.2. Photometry and astrometry

The planet β Pictoris b is detected in the J band with the RADI, LOCI, and KLIP algorithms (see Fig. 1). We also retrieved the planet in our two epochs H band data and single epoch M' band data. We find nominal SNR of 8, 17, 23, and 11 with LOCI on the three set of data (for separation criteria of 1.00, 1.00, 0.75, and $0.5 \times FWHM$ respectively). To compute these SNR, we measured the signal in a circular aperture (3-pixels in radius) centered on the planet. The noise per pixel was estimated on a ring at the same radius (but excluding the planet) and translated to the same surface as the circular aperture (quadratically).

The position and flux of the planet is affected by the inevitable partial point source self-subtraction occurring in ADI (Lafrenière et al. 2007; Marois et al. 2010a; Bonnefoy et al. 2011). We estimated the level of self-subtraction by injecting artificial planets in the raw frames built from renormalized unsaturated exposures of the star taken before and after the sequence of saturated exposures. We first injected artificial planets at seven different position angles (256, 301, 346, 31, 76, 121, and 166°) and different positive fluxes (flux ratio from 1×10^{-5} to 1×10^{-4} for the J band, and 5×10^{-5} to 1.5×10^{-4} for the H band) at the guessed planet separation in the raw J and H band data and applied the ADI algorithms. We repeated this procedure in the M' band but considered only three position angles (32, 122, 302°) to avoid a cross-contamination of the angular-differential imaging pattern induced by the artificial planets. We then compared the flux of β Pictoris b integrated over a circular aperture (radius of 3 pixels) to those of artificial planets in order to calibrate the self-subtraction (hereafter $FPPOS$). We also

---

[1] We retrieve the sideral time at Paranal (LST) from the Universal Time. The LST and target coordinate is used to derive the hour angle. The hour angle is then converted to parallactic angle.

Table 2. Photometric measurements of β Pictoris b.

Obs. date	Filter	Methods	Contrast (mag)
16/12/2011	J	RADI	10.4 ± 0.5
16/12/2011	J	LOCI	10.5 ± 0.3
16/12/2011	J	KLIP	10.8 ± 0.3
18/12/2011	H	CADI	9.9 ± 0.3
18/12/2011	H	RADI	10.2 ± 0.4
18/12/2011	H	LOCI	9.9 ± 0.3
11/01/2012	H	CADI	10.1 ± 0.3
11/01/2012	H	RADI	10.0 ± 0.2
11/01/2012	H	LOCI	9.9 ± 0.2
11/01/2012	H	KLIP	10.0 ± 0.3
26/11/2012	M'	CADI	7.5 ± 0.3
26/11/2012	M'	RADI	7.5 ± 0.3
26/11/2012	M'	LOCI	7.6 ± 0.3
26/11/2012	M'	KLIP	7.8 ± 0.3

Table 3. Astrometry of β Pictoris b for the H-band data obtained on January 11, 2012.

UT Date	11/01/2012
True North[a]	-0.53 ± 0.03 deg
Platescale[a]	13.22 ± 0.02 mas
Rotator offset	90.46 ± 0.10 deg
ΔRA	-241 ± 13 mas
ΔDec	-387 ± 14 mas
Separation	456 ± 11 mas
PA	211.89 ± 2.32 deg

Notes. [a] Derived from observations of the Theta Ori C astrometric field (ESO Large Program 184.C-0567) taken in the H band with the S13 camera on January 2, 2012.

followed an alternative approach injecting artificial planets one by one with negative fluxes at the companion position (*FPNEG* Bonnefoy et al. 2011; Chauvin et al. 2012). We retrieved the flux of β Pictoris b minimizing the standard deviation of the residuals at the injection position for each injection flux. We finally derived contrast values using the estimated flux of β Pictoris b, the flux of the unsaturated frames corrected from the transmission of the neutral density filters and renormalized to the integration time of the saturated exposures. We give transmissions of NaCo neutral densities for the J, H, $K_{\rm s}$, L', and M' band filters that we measured from on-sky data for that purpose in Appendix A. We repeated the procedure for the CADI, RADI, LOCI algorithms using six separation criteria (0.25, 0.5, 0.75, 1, 1.25, and $1.5 \times FWHM$ respectively) and with the KLIP algorithm keeping only the 10 and 20 first Karhunen-Loève transforms of the references images ($K_{\rm KLIP}$ parameter). *FPPOS* and *FPNEG* give similar contrasts when used with LOCI. Nevertheless, the level of self-subtraction with LOCI is not expected to vary linearly with the injection flux and could bias the contrast derived with *FPNEG*. We then chose to conserve the contrast values derived from *FPPOS* with LOCI alone.

The mean contrast values for each ADI algorithm are reported in Table 2. The error is dominated by the variation in the flux of unsaturated exposures (variable Strehl ratio and atmospheric transmission). KLIP confirms previous contrast estimates found with CADI, RADI, and LOCI. The algorithm could provide a more accurate estimate of the planet contrast. Nevertheless, it has not been extensively tested on NaCo data yet. We chose not to use the corresponding contrast values in the following analysis.

We extracted the position of the planet with respect to the star in the high signal-to-noise residual frames obtained from January 2012 data using the *FPNEG* method described in Chauvin et al. (2012). Results are reported in Table 3. We used the instrument True North and Platescale values derived from observations of the Θ Ori C astrometric field (McCaughrean & Stauffer 1994). The uncertainty on the star center dominates the final error budget. We analyze this new astrometry and its implication on the orbital parameters of β Pictoris b in Sect. 4.3.

4. Results

We derived contrasts of $\Delta H = 10.0 \pm 0.2$ mag and $\Delta M' = 7.5 \pm 0.2$ mag for β Pictoris b (see Table 2). The

planet is detected at a lower SNR in the J band when using RADI ($SNR \leq 6$). For this reason, we decided to retain the photometric measurement obtained with LOCI only in this band for the following analysis ($\Delta J = 10.5 \pm 0.3$ mag).

We converted the ESO J and H-band photometry of β Pictoris (van der Bliek et al. 1996a) to the 2MASS photometric system ($J = 3.524 \pm 0.013$ mag, $H = 3.491 \pm 0.009$ mag) using the color transformations of Carpenter (2001). We estimate that the magnitude difference between 2MASS and NaCo systems for an A6 star is less than 0.002 mag using the mean spectrum of A5V and A7V stars of the Pickles (1998) library, a flux-calibrated spectrum of Vega (Bohlin 2007), and the corresponding filter passbands. We then measure $J = 14.0 \pm 0.3$ and $H = 13.5 \pm 0.2$ for β Pictoris b. This corresponds to absolute magnitudes $M_J = 12.6 \pm 0.3$ mag and $M_H = 12.0 \pm 0.2$ mag at 19.44 ± 0.05 pc (van Leeuwen 2007). We combined the M' band contrast of β Pictoris b we obtained to the star magnitude ($M = 3.458 \pm 0.009$; Bouchet et al. 1991) and derived $M' = 11.0 \pm 0.2$ mag and $M_{M'} = 9.5 \pm 0.3$ mag. Currie et al. (2011b) have previously derived a photometry of the planet at M' band (4.98 μm) from ADI observations. We did not use this photometric data point as comparison since the dataset was missing unsaturated exposures. Without this calibration, it is not possible to properly estimate the level of self-subtraction associated to the data reduction method

We use this new photometry and the one reported in Quanz et al. (2010) and Bonnefoy et al. (2011) for the $K_{\rm s}$ (2.18 μm), L' (3.8 μm), and NB_4.05 (4.05 μm) filters for the following analysis. It is summarized in Table 7.

4.1. Empirical comparison

4.1.1. Color–color diagrams

We overlaid β Pictoris b colors on $J - H$ vs. $H - K_{\rm s}$ diagrams in Fig. 2 along with additional field-dwarf objects (Burgasser et al. 2006; Reid et al. 2008; Dupuy & Liu 2012) and low-mass companions (see Table B.1 for a description of the objects). We also overlaid the colors of M8.5$_\gamma$–L5$_\gamma$ dwarfs having spectral features indicative of reduced surface gravity and likely or confirmed members of young nearby associations (Looper et al. 2007; Rice et al. 2010; Faherty et al. 2013, and reference therein). β Pictoris b has colors compatible with field L dwarfs and redder than T dwarfs. The comparison also reveals that the L5$_\gamma$ and most of the L4$_\gamma$ dwarfs are redder than the planet. β Pictoris b colors are close to those of late-M/early-L companions TWA 5B,

USCO CTIO 108B, GSC 06214-00210 b, 1RXS J160929.1-210524 b, and CD-35 2722B in addition to κ And b in the diagram.

We reach different conclusions when comparing the L' and M' band-based colors of β Pictoris b to those of mature M, L, T field dwarfs (Golimowski et al. 2004), and young companions or binaries in Fig. 3. β Pictoris b colors are compatible with those of mid-L to T field dwarfs in the three diagrams. The companion $K_s - L'$ color is ~1 mag redder than those of late-M field dwarfs. The planet has $J - H$ and $J - K_s$ colors that are bluer than most of the young companions with the exception of κ Andromedae, 1RXS J160929.1-210524 b, and HR 8799c. The origin of this apparent inconsistency is discussed in Sect. 5.1.

4.1.2. Color–magnitude diagrams

The planet is more easily distinguished from comparison objects (mature or young field dwarfs and young companions) in color−magnitudes diagrams (Figs. 4 and 5). It lies in the middle of the sequence of field L-dwarfs in the diagrams.

The two other late-M (M5-M9) brown dwarf companions orbiting stars of the β Pictoris moving group, PZ Tel b (Biller et al. 2010) and HR 7329 B (Lowrance et al. 2000), are more luminous and bluer than the planet. This is consistent with β Pictoris b being less massive and cooler than these objects. In the diagrams, we report the photometry of other planet/brown-dwarf companions to massive stars. The planet/brown-dwarf companion recently imaged around the ~30 Myr old star κ And b (Carson et al. 2013) falls at close positions in color–magnitude diagrams ($JHKL'$) as β Pictoris b. The good match in colors is consistent with "hot-start" evolutionary models predictions that give close T_{eff} (~1700 K) for the (close) observed luminosity of these companions. Conversely, the late-L/early-T exoplanets HR 8799 bcde (Marois et al. 2008, 2010b) are all at distinct positions than β Pictoris in these diagrams. This agrees with the HR 8799 system (30 Myr, Columba association, Zuckerman et al. 2011) being older and the planets cooler than β Pictoris b.

We also show in these figures the photometry of the young M_γ and L_γ dwarfs with measured parallaxes (Faherty et al. 2012, 2013). β Pictoris is fainter than $M8.5_\gamma - M9_\gamma$ dwarfs, and among them is 2MASS J060852832753583, the currently lowest mass, isolated member of the β Pictoris moving group (Rice et al. 2010). The planet is more luminous than the $L4_\gamma$ (2MASS J05012406-0010452) and $L5_\gamma$ (2MASS J035523.51+113337.4) dwarfs. Interestingly, β Pictoris b and κ And b are close to the $L0_\gamma$ dwarf 2MASS J00325584-4405058 in these diagrams. We recently confirm the optical classification (Cruz et al. 2009) and the presence of peculiar spectral features in the near-infrared spectrum of this object. 2MASS J00325584-4405058 might then be a valuable proxy of the spectroscopic properties of β Pictoris b and κ And b. We can then conclude from this empirical analysis that most of β Pictoris b photometric properties are similar to those of early-L (L0-L4) dwarfs.

We used this crude constraint on the spectral type of the planet to derive a luminosity estimate. Faherty et al. (2013) show that the SED of young L-type dwarfs can deviate significantly from those of mature field dwarfs with similar spectral types. We instead estimated a $BC_K = 3.22 \pm 0.16$ mag for β Pictoris b, taking the mean of the bollometric corrections measured for the young L0 dwarf 2MASS J01415823-4633574 and L5 dwarf 2MASS J035523.37+113343.7 (3.39 and 3.06 respectively; Todorov et al. 2010; Faherty et al. 2013). We used this correction
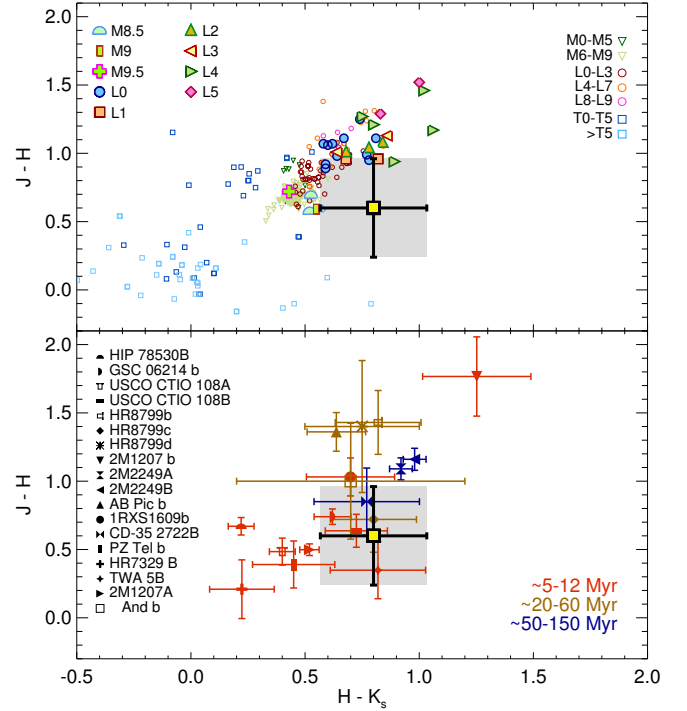

Fig. 2. Location of β Pictoris b (yellow square) in a $J - H$ versus $H - K_s$ color–color diagrams.

to derive a luminosity $\log_{10}(L/L_\odot) = -3.87 \pm 0.08$ mag for β Pictoris b.

4.2. Spectral synthesis

We compared β Pictoris b fluxes to synthetic photometry generated from seven atmospheric models. All models make use of the multipurpose radiative-transfer code PHOENIX (Hauschildt & Baron 1999; Hauschildt 1999) assuming 1D radiative transfer, hydrostatic equilibrium, convection based on the mixing length theory, chemical equilibrium, and an opacity sampling treatment of the opacities. PHOENIX computes the emerging flux at the top of the photospheric layers at given wavelengths for a grid of effective temperatures (T_{eff}), surface gravities (log g), and metallicities ([M/H]). Integrated surface fluxes and magnitudes were derived for each combinasion of atmospheric parameter (T_{eff}, log g, [M/H]) using the corresponding model spectra, the NaCo filter passbands, and a flux-calibrated model spectrum of Vega (Bohlin 2007). Model fluxes were multiplied by the dilution factor R^2/d^2 (with R and d the radius and distance of the object respectively) to match the apparent fluxes of β Pictoris b. Our spectral synthesis tool then retrieved T_{eff}, log g, and R simultaneously minimizing the χ^2 with the planet flux. The analysis was conducted with solar-metallicity models. We also explored the effects of the metallicity on the determination of T_{eff} and log g with the DRIFT-PHOENIX and BT-Settl 2012 models.

The empirical study presented in Sect. 4.1 and previous temperature estimates (Bonnefoy et al. 2011; Currie et al. 2011b) suggest that clouds of silicate dust are present in the atmosphere of the planet. The PHOENIX models used in the following sections explore different cloud formation conditions.
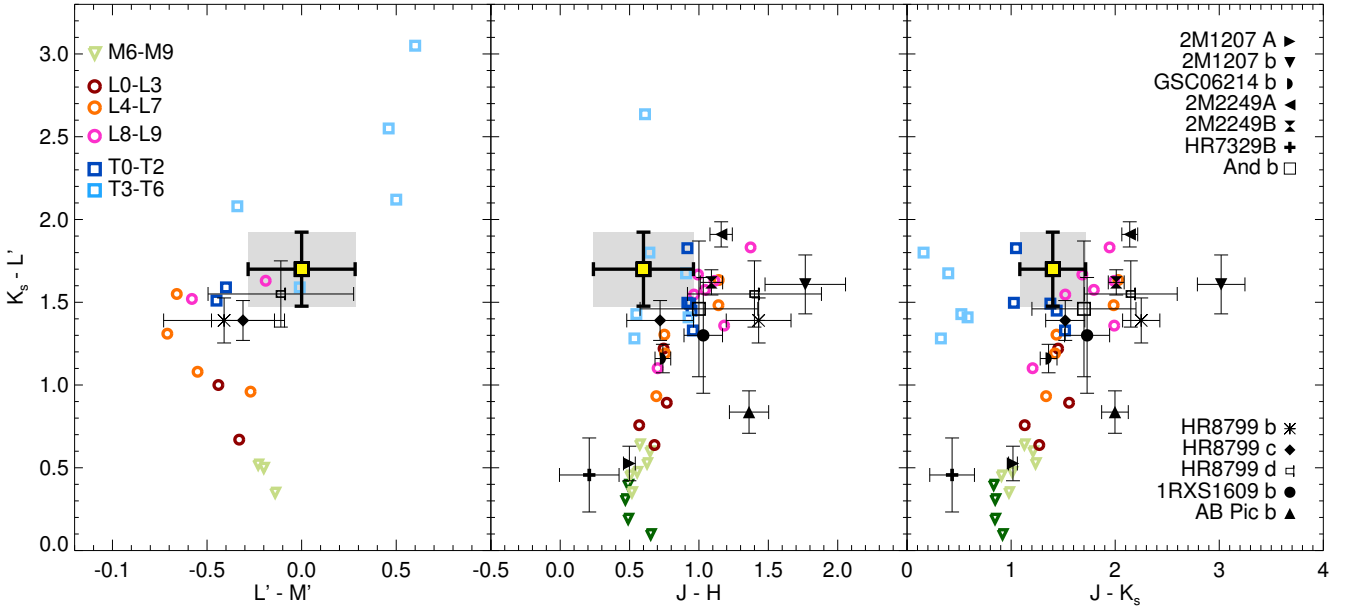
Fig. 3. Location of β Pictoris b (yellow square) in $K_s - L'$ versus $L' - M'$ (*left panel*), $J - H$ (*middle panel*), and $J - K_s$ (*right panel*) color–color diagrams with respect to field M (open triangles), L (open circles), and T (open squares) dwarfs. colors of known young objects (companions, binaries) with available L'-band and M'-band photometry are overlaid.
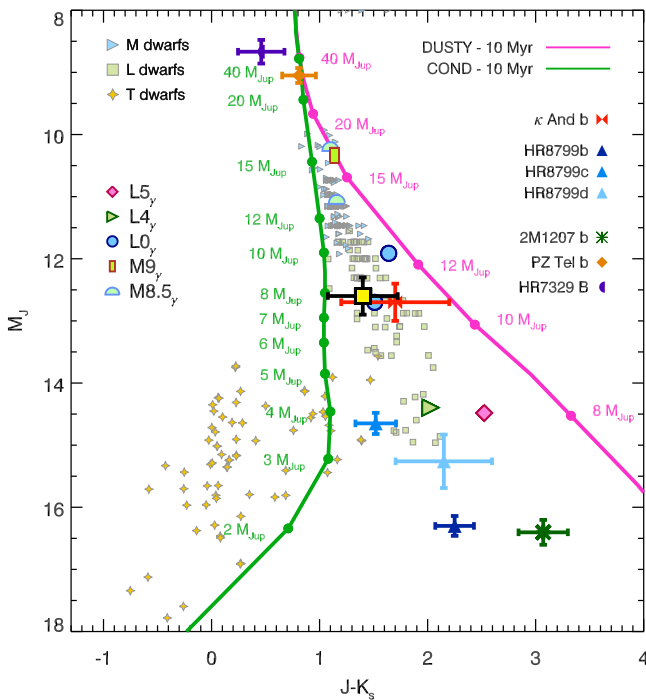

Fig. 4. β Pictoris b (yellow square) in an M_J versus $J - K_s$ color–magnitude diagram.
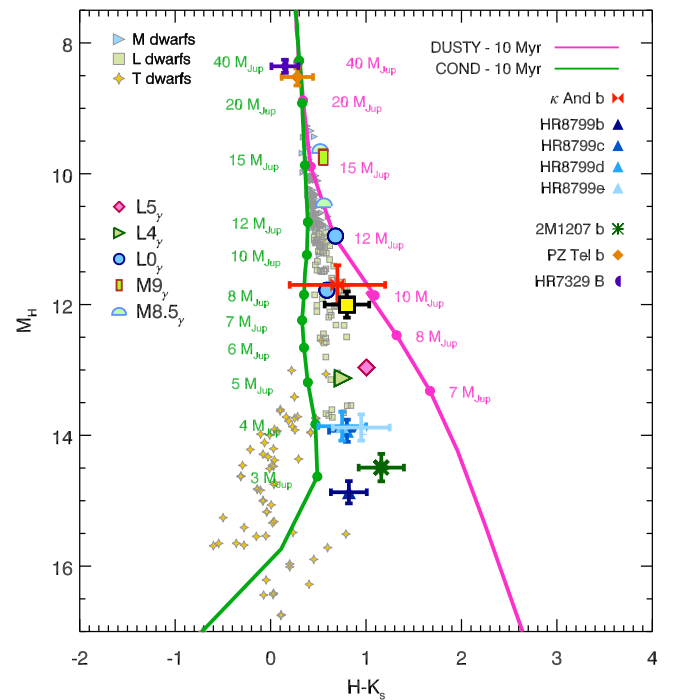
Fig. 5. Same as Fig. 4 but for M_H versus $H - K_s$

4.2.1. AMES-Dusty and AMES-Cond

AMES-Dusty/Cond (Allard et al. 2001) atmospheric models used PHOENIX to solve the plan-parallel radiative transfer, together with the Nasa AMES TiO and H_2O molecular line lists (Allard et al. 2000). Models relied on the solar abundances by Grevesse et al. (1993). These models explored the limiting conditions of dust formation for 30 types of grains in phase equilibrium. The AMES-Dusty models simulate the case of maximum dust formation where the sedimentation (or gravitate settling) is neglected. The AMES-Cond models consider the opposite case

where dust forms and is immediately rained-out from the photosphere, producing the depletion of the elements. The grain opacities are obtained by solving the Mie equation for spherical grains and assuming the interstellar grain size distribution, using complex refraction index of materials as a function of wavelength compiled by the Astrophysikalisches Institut und Universitäts-Sternwarte in Jena.

We showed in Bonnefoy et al. (2010) that AMES-Dusty models do not simultaneously reproduce the pseudo-continuum and the water-band absorptions of the near-infrared (1.1−2.5 μm) spectrum of the L-type planet/brown-dwarf

Table 4. Best-fitted atmospheric parameters for β Pictoris b.

Atmospheric model	T_{eff} (K)	$\log g$ $\log(\text{cm s}^{-2})$	Radius (R_{Jup})	χ^2
AMES-Dusty	1700	3.5	1.22	4.96
AMES-Cond	1400	3.5	1.89	8.04
BT-Settl 2010	1600	3.5	1.61	2.99
BT-Cond 2012	1800	4.0	1.16	17.80
BT-Dusty 2012[a]	1700:	4.5:	1.76:	3.08
BT-Settl 2012 [M/H] = 0.0	1700	3.5	1.29	4.27
BT-Settl 2012 [M/H] = +0.5	1600	4.5	1.43	5.45
DRIFT-P. [M/H] = 0.0	1700	4.0	1.38	2.02
DRIFT-P. [M/H] = +0.5	1700	4.0	1.38	3.06
DRIFT-P. [M/H] = −0.5	1700	4.0	1.38	2.14

Notes. [a] Analysis limited to $\log g \geq 4.5$.

companion AB Pic b. β Pictoris b is expected to lie in the same temperature range (Bonnefoy et al. 2010, 2013b). Our analysis could then be similarly affected by this bias. Nevertheless, AMES-Dusty and AMES-Cond models are used as boundary conditions of the evolutionary models of Chabrier et al. (2000) and Baraffe et al. (2003). We therefore used them to determine T_{eff}, $\log g$, and radius estimates in order to preserve the self-consistenty in Sect. 4.4.1.

We selected a subgrid of synthetic spectra with $1000\,\text{K} \leq T_{\text{eff}} \leq 3000\,\text{K}$, $3.5 \leq \log g \leq 6.0$. Best-fitted atmospheric parameters and radii are reported in Table 4. We show in Fig. 6 the best-fitted fluxes and the corresponding synthetic spectra. Models reproduce β Pictoris b photometry for close T_{eff} (see Table 4). However, the quality of the fit as expressed by low χ^2 values is significantly better using the AMES-Dusty models. Visually (Fig. 6), the J-band flux of β Pictoris b is midway between those of best-fit AMES-Cond and AMES-Dusty models. The remaining photometric points of the planet are reproduced better by the AMES-Dusty models, with the exception of the L' band (discussed in Sect. 5.1). In general, AMES-Cond models produce an SED slope that is too blue compared to the planet. Both best-fit AMES-Cond/Dusty spectra fall at the edge of the range of surface gravities covered by the grids of models. The χ^2 map of the AMES-Cond models suggest that the fit could still be improved for lower surface gravities for the same temperature. The corresponding map for AMES-Dusty models shows the fit is mostly sensitive to the effective temperature (Fig. 7).

4.2.2. BT-Settl, BT-Cond, and BT-Dusty models

Unlike AMES-Dusty/Cond atmospheric models, BT-Settl models (Allard et al. 2003) use a cloud model to predict the number density and size distribution of dust grains across the 1D atmosphere. These models use the Rossow (1978) cloud model, which compares the timescales of the main processes (mixing, sedimentation, condensation, coalescence, and coagulation) layer-by-layer. The mixing timescales are derived from Radiation HydroDynamic (RHD) simulations (Freytag et al. 2010). For the 2010 prerelease of the BT-Settl models (Allard et al. 2011) (hereafter BT-Settl 2010), the cloud model was improved by a dynamical determination of the supersaturation – the ratio of the saturation vapor pressure to the local gas pressure $P_{\text{sv}}/P_{\text{g}}(t)$. In the 2012 prerelease of the BT-Settl models (Allard et al. 2012; Allard & Homeier 2012, hereafter BT-Settl 2012) the cloud model was further improved by the implementation of
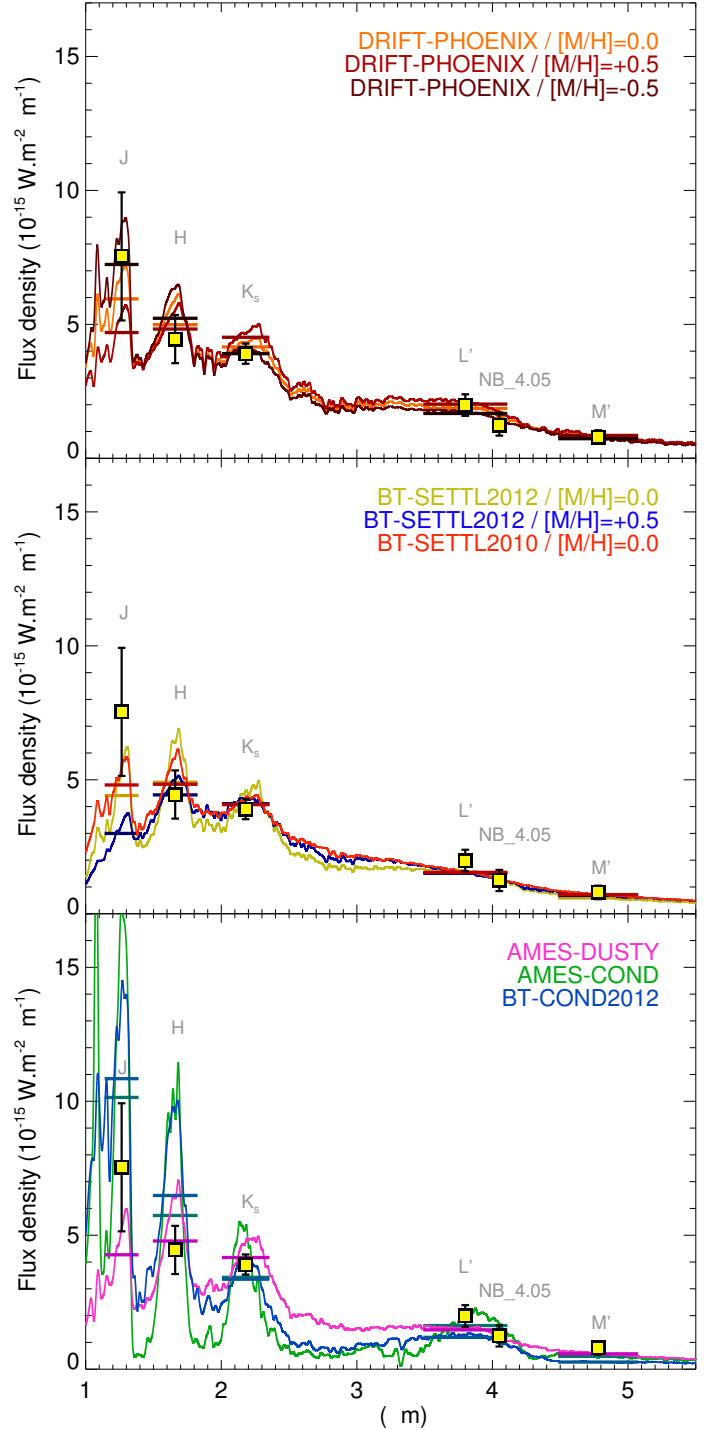

Fig. 6. Comparison of the apparent fluxes of β Pictoris b (yellow squares) to best fitted fluxes (horizontal barres) generated from synthetic spectra. *Bottom*: comparison to AMES-Cond (green; T_{eff} = 1400 K, $\log g$ = 3.5, and R = 1.89 R_{Jup}), AMES-Dusty (pink; T_{eff} = 1700 K, $\log g$ = 3.5, and R = 1.22 R_{Jup}), and BT-Cond2012 (blue; T_{eff} = 1800 K, $\log g$ = 4.0, and R = 1.16 R_{Jup}) synthetic fluxes/spectra. *Middle*: comparison to BT-Settl 2012 models at solar metallicity (gold; T_{eff} = 1700 K, $\log g$ = 3.5, and R = 1.29 R_{Jup}), to BT-Settl 2012 models with [M/H] = +0.5 dex (blue; T_{eff} = 1600 K, $\log g$ = 4.5, and R = 1.43 R_{Jup}), and to BT-Settl 2010 (red; T_{eff} = 1600 K, $\log g$ = 3.5, and R = 1.61 R_{Jup}) synthetic fluxes at solar metallicity. The corresponding model spectra smoothed at the resolution of the NB_4.05 filter are also shown. *Top*: comparison to DRIFT-PHOENIX spectra (T_{eff} = 1700 K, $\log g$ = 4.0, and R = 1.38 R_{Jup}) with solar metallicity (M/H = 0.0, orange), metal-enriched (M/H = +0.5, dark red), and metal-depleted (M/H = –0.5, brown) atmospheres.
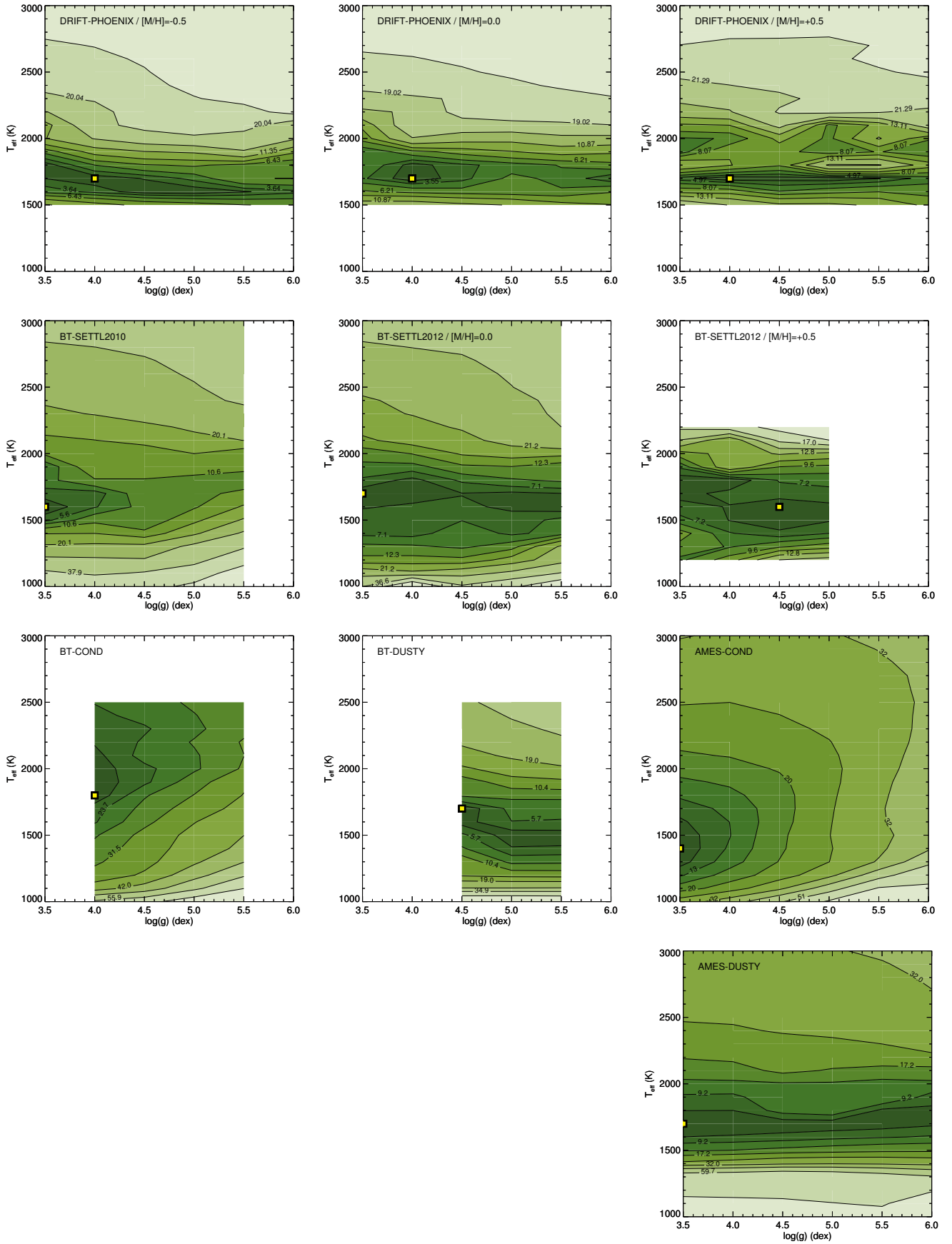
Fig. 7. χ^2 maps obtained when comparing the spectral energy distribution of the planet to synthetic fluxes derived from atmospheric models for given $\log g$ and $T_{\rm eff}$. Minima are indicated by yellow squares.

a grain size-dependent forward scattering and by accounting for nucleation based on cosmic ray studies (Tanaka 2005). These latter change allowed the cloud model to limit its refractory element depletion and form relatively more dust grains in higher atmospheric layers.

The cloud model is solved from the innermost to the outermost atmospheric layers, depleting the gas composition due to sedimentation gradually from the bottom to the top of the atmosphere. This model obtains both the density distribution of grains and the grain average size per layer, and includes 55 types of grains (including metal, ceramic, salt, and ice crystals). The BT-Settl models do not assume a seed composition since the cloud model modifies the equilibrium chemistry iteratively at each atmospheric layer. The resulting number density of dust grains is not in phase equilibrium, even if the equilibrium chemistry is used to adjust the gas phase abundances layer-by-layer.

The BT-Settl models are computed with the PHOENIX stellar atmosphere code using the spherical radiative transfer. The code use up-to-date molecular line list of the water vapor (BT2, Barber et al. 2006), CH_4 (Homeier 2005), CIA of H_2 (Borysow 2002), TiO, VO, MgH, CrH, FeH, and CaH (Plez 1998; Weck et al. 2003; Dulick et al. 2003), and new alkali-line profiles (Allard et al. 2007). The nonequilibrium chemistry for CO, CH_4, CO_2, N_2, and NH_3 is also included based on the RHD simulation results (Freytag et al. 2010). Finally, the models rely on the revised solar abundances (Grevesse (2009) for the BT-Settl 2010 models and Caffau et al. (2011) for the BT-Settl 2012 models), which translates into less pronounced water-band absorptions and redder colors in the near-infrared than previous version of the models (e.g. those used in Allard et al. 2007; Bonnefoy et al. 2010).

We demonstrate in Bonnefoy et al. (2013a) that the BT-Settl 2010 models self-consistently represent the optical and near-infrared spectra, together with the Spitzer photometry ($3.6-8$ μm) of the young (1–3 Myr) M9.5 dwarf KPNO-Tau-4 (Briceño et al. 2002). They should then be appropriate for β Pictoris b given the spectral type and age range of the planet. We compared β Pictoris b photometry with the models for 1000 K $\leq T_{\rm eff} \leq 3000$ K an $3.5 \leq \log g \leq 5.5$. We plot the best-fit model fluxes and corresponding synthetic spectra in Fig. 6. Our fitting procedure gives close (± 100 K) effective temperatures to the AMES-Dusty models. The χ^2 is reduced compared to previous models, given the better agreement of the predicted J band flux with the one of the planet (Figs. 7 and 6).

BT-Settl 2012 models at solar metallicity ([M/H] = 0) with 1000 K $\leq T_{\rm eff} \leq 3000$ K and $3.5 \leq \log g \leq 5.5$ were first considered here. We also used a subgrid of metal-enriched models ([M/H] = +0.5) for 1200 K $\leq T_{\rm eff} \leq 2000$ K and $3.5 \leq \log g \leq 5.0$. Revised versions of the Cond and Dusty models (hereafter BT-Cond/Dusty 2012) were calculated using the same opacities and solar abundances as for the BT-Settl 2012 models for comparison. BT-Cond 2012 and BT-Dusty 2012 models were only computed on a restricted grid of parameters at the time of the analysis. Consequently, the analysis with the BT-Cond 2012 models was limited to 1000 K $\leq T_{\rm eff} \leq 2500$ K, $4.0 \leq \log g \leq 5.5$, and [M/H] = 0. The BT-Dusty 2012 model grid was also restrained to the same temperature range, [M/H] = 0, and $\log g \geq 4.5$ dex. Log $g = 4.5$ falls above the surface gravity expected for β Pictoris b (see Sect. 4.4.1) and found using BT-Settl 2010 and AMES models. We then only used BT-Dusty 2012 models to provide an additional check of the atmospheric parameters found using other models.

Parameters of best-fitted 2012 models are reported in Table 4. In Fig. 6, we also overlaid the synthetic spectra and

fluxes of the BT-Cond 2012 and BT-Settl 2012 models. The analysis confirms trends seen with the other models. The χ^2 maps all show a clear minimum for $T_{\rm eff}$ = 1600–1800 K (Fig. 7). Best fits are found for reduced surface gravities compared to those determined for mature field dwarfs ($4.5 \lesssim \log g \lesssim 6$, see Testi 2009). We note, however, that the χ^2 map corresponding to the BT-Settl 2012 models still shows a weaker contraint on $\log g$ than on $T_{\rm eff}$. BT-Settl 2012 models reproduce the planet photometry better. Metallicity changes $T_{\rm eff}$ estimate by only 100 K. The BT-Cond 2012 model predict bluer colors than the planet. BT-Dusty 2012 models give the lowest χ^2 despite the limited interval of $\log g$ of the model. The fit with BT-Settl 2012 models has a higher χ^2 than obtained from the BT-Settl 2010 models. We discovered with visual inspection that the fit is indeed degraded in the J band.

4.2.3. DRIFT-PHOENIX models

The DRIFT-PHOENIX models couple the PHOENIX code to a nonequilibrium cloud model DRIFT (Woitke & Helling 2003, 2004; Helling & Woitke 2006; Helling et al. 2008b), which accounts for the nucleation, seed formation, growth, evaporation, gravitational settling, and advection of a set of grains. The general differences between these models and the 2008 version of the BT-Settl models are given in Helling et al. (2008a). We note that the models use older reference solar abundances (Grevesse et al. 1993, also used in AMES-Dusty/Cond models) than those of the 2010–2012 releases of the BT-Settl models.

The grid of synthetic spectra extends from 1500 to 3000 K with $3.0 \leq \log g \leq 6.0$. The grid was computed for three different metallicities (M/H = –0.5, 0, and +0.5 dex). We showed in Bonnefoy et al. (2013b) that these models give a correct representation of the near-infrared spectra and SED of young M and early-L dwarfs.

Results of the fit are also reported in Table 4 and shown in Fig. 6. The fit confirms the effective temperature and low surface-gravity estimates derived with the other models. The χ^2 maps indicate fits are sensitive to the effective temperature and do not enable an accurate constraint on the surface gravity. The metallicity does not bias the determination of the effective temperature. Models with solar abundances still match the planet photometry best.

We conclude that the PHOENIX-based models used above predict $T_{\rm eff} = 1700 \pm 100$ K for β Pictoris b. The SED seems to be systematicaly best reproduced by the models with $\log g = 4.0 \pm 0.5$ dex. We note, however, that this parameter is less constrained than the effective temperature. The analysis also demonstrates that once dust is present in the cloud models, our fit provides close effective temperature and surface gravity estimates despite the different underlying physics used in the models. We adopt a radius of $R = 1.4 \pm 0.2$ $R_{\rm Jup}$ for the planet based on the scaling factors between the DRIFT-PHOENIX, BT-Settl, and BT-COND models and the observations. These temperatures and radii correspond to a luminosity $\log_{10} (L/L_\odot) = -3.83 \pm 0.24$ dex (Stephan-Boltzmann law). This value is consistent with the empirical luminosity derived in Sect. 4.1.2. We use the latter for the following analysis.

4.3. Orbital parameters

We combined our new astrometric data point to those reported in Chauvin et al. (2012) and fit orbits using a Levenberg-Marquardt algorithm (LSLM) and Markov chain Monte Carlo (MCMC)
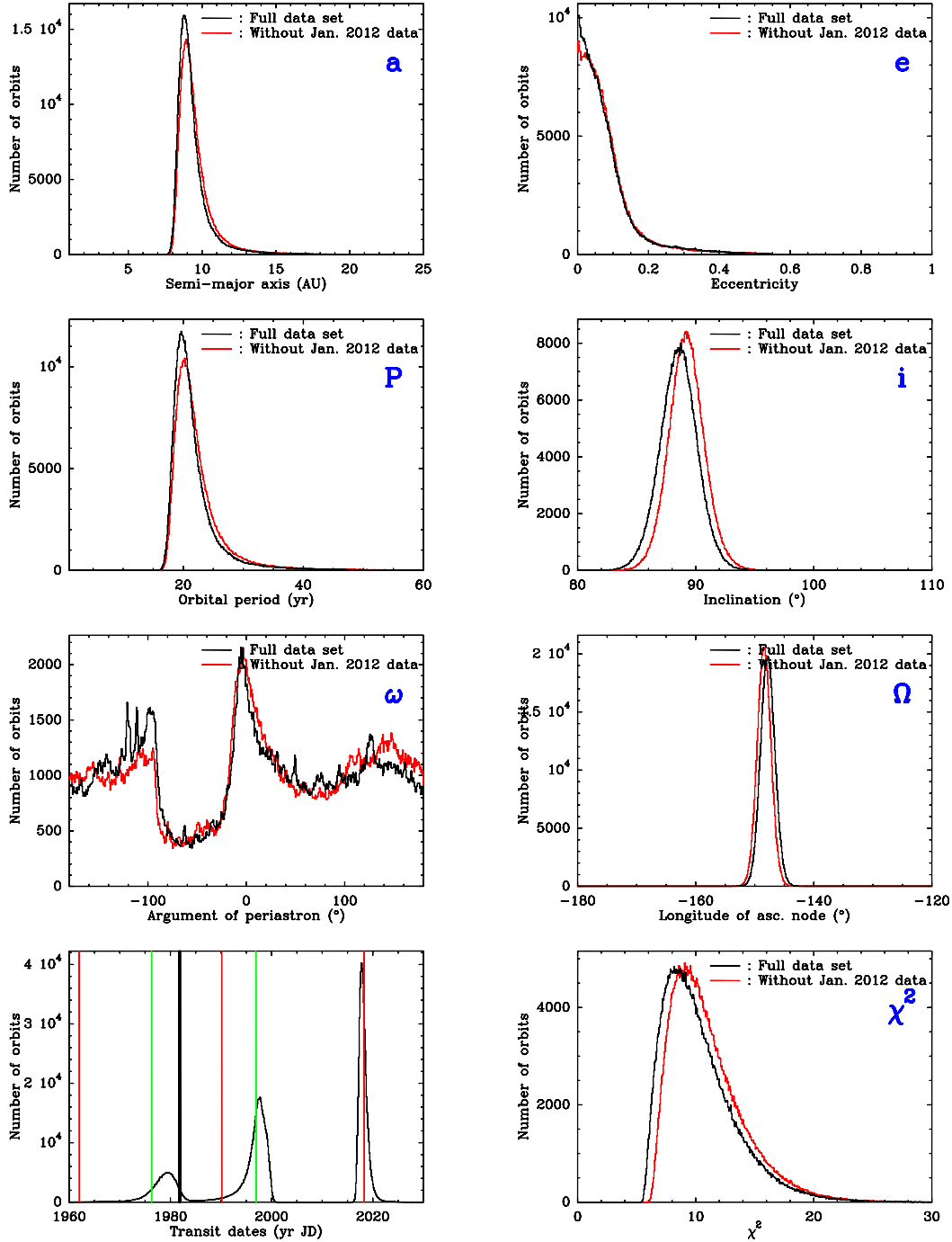
Fig. 8. Distribution of orbital parameters from the MCMC fit of the set of astrometric data from Chauvin et al. (2012) (black), including the new astrometric data point gathered from the new *H*-band data (red; see Sect. 3.2). *Top row*: semi-major axis *a* (*left*) and *e* (*right*). *Third row bottom*: period *P* (*left*) and inclinaison *i* (*right*). *Second row from bottom*: argument of periastrom ω (*left*) and longitude of ascending node Ω (*right*). *Bottom row*: transit date (*left*) and distribution of χ^2. Red bars correspond to parameters found from the best LSLM χ^2 model. Green bars correspond to highly probable orbital parameters derived from the MCMC approach. The 1981 photometric events is reported as a thick black bar in the bottom-left diagram.

simulations as described in the aforementioned study, but yet with an improved algorithm. The results of MCMC simulations are reported in Fig. 8, superimposed with new simulations performed with the same dataset without the new January 2012 astrometric point. The improvement in the probability curves with respect to Chauvin et al. (2012) is noticeable, even in the simulations using the old dataset. This is due to the improvement of the MCMC sampling algorithm. This way we can clearly see what the new point bears.

The main results from Chauvin et al. (2012) are nevertheless confirmed. The semi-major axis of β Pictoris b falls in the 8−10 AU range with a probability higher than 80%. Subsequently, the orbital period ranges between 17 and 25 years with the same probability. The planet eccentricity is ≲0.15 with similar probability. Apart from the 2003 point, our astrometric points are all located on one side of the star, and span a rather limited amount of time. Therefore, eccentric orbits with long periods and that are currently passing at periastron cannot be

excluded. It is also not yet possible to state whether the eccentricity is zero of not. The argument of periastron is then badly constrained, apart from a peak appearing around $\omega = 0$.

Conversely, the orbital inclination and the longitude of ascending node Ω are well constrained parameters, even if the addition of the 2012 point causes a small shift in the MCMC distributions. We confirm the edge-on orientation of the orbit within $\lesssim 4°$ with a probability higher than 90%. We also confirm that the orbit is more probably slightly viewed as prograde ($i < 90°$) rather than retrograde. The longitude of ascending node is confined to the range 145–150° with similar probability. Due to the edge-on orientation of the disk, this parameter is closely related to the PA of the disk. We confirm here the analysis of Lagrange et al. (2012a), who demonstrate that the orbital plan of β Pictoris b was located in the midplane of the inner disk rather than in that of the main disk. This supports the model of Mouillet et al. (1997) and Augereau et al. (2001), who attributed the disk warp to the perturbing action of an inner giant planet, which thus could correspond well to β Pictoris b.

Similarly, we computed the MCMC distribution of the possible transit passages of the planet (Fig. 8). We also confirm that the putative transit date of Nov. 1981 claimed by Lecavelier Des Etangs & Vidal-Madjar (2009) could still be due to β Pictoris b, since the quoted date still falls in a peak of the distribution. Meanwhile, our analysis predicts a possible next transit in 2018, which will deserve to be observed.

The falling evaporating bodies (FEBs) scenario (Beust & Morbidelli 1996, 2000; Beust et al. 2001) also predict the presence of a Jovian-sized planet at ~10 AU as responsible for the infall of numerous star-grazing planetesimals (FEBs) via its inner mean-motion resonances. Obviously, β Pictoris b could correspond to this planet. However, a major requirement of the FEBs model is that the suspected planet is slightly eccentric ($e \gtrsim 0.05$) with a convenient orientation of its periastron with respect to the line of sight. The paucity of our data means it is still not possible to state whether β Pictoris b fulfills this condition. This motivates us to continue monitoring the orbit. The peak that appears at $\omega \simeq 0°$ and that corresponds to orbits with some eccentricity, is nevertheless interesting. As noted in Chauvin et al. (2012), the orientation of the planet periastron required by the FEB scenario translates into $0 \lesssim \omega \lesssim 20°$. The presence of the peak close to this range in the ω distribution is encouraging.

These up-to-date constraints on the orbital parameters of β Pictoris b combined with the present constraints coming from radial velocity measurments (Lagrange et al. 2012b) confirm the upper limits of 12 and 15.5 M_{Jup} on the planet mass for semi-major axis of 9 and 10 AU, respectively. We compare these dynamical constraints to evolutionary model-dependent masses in the following section.

4.4. New mass estimates

We used evolutionary models that couple nongray radiative-convective atmosphere models to thermal evolution models based on different intial conditions to estimate new physical parameters (mass, T_{eff}, log g, radius) for the planet.

4.4.1. Hot-start and cold-start evolutionary tracks

We first considered the DUSTY and COND evolutionary tracks of Chabrier et al. (2000) and Baraffe et al. (2003) to derive the mass, T_{eff}, log g, and radius of the planet (Table 5) using the photometry in each bands, the luminosity, or the temperature

Table 5. Masses, T_{eff}, surface gravity, and radii estimated from hot-start evolutionary models.

Model	Input	Mass (M_{Jup})	T_{eff} (K)	log g log (cm s^{-2})	Radius (R_{Jup})
DUSTY	M_J	$10.4^{+2.7}_{-1.3}$	1720^{+65}_{-39}	$4.04^{+0.13}_{-0.07}$	$1.53^{+0.05}_{-0.09}$
DUSTY	M_H	$9.2^{+3.0}_{-1.1}$	1615^{+53}_{-38}	$4.00^{+0.16}_{-0.05}$	$1.50^{+0.04}_{-0.09}$
DUSTY	M_{K_s}	$8.4^{+3.3}_{-1.1}$	1537^{+79}_{-42}	$3.98^{+0.18}_{-0.07}$	$1.48^{+0.03}_{-0.09}$
DUSTY	$M_{L'}$	$9.8^{+3.8}_{-2.5}$	1674^{+177}_{-176}	$4.02^{+0.14}_{-0.09}$	$1.52^{+0.07}_{-0.10}$
DUSTY	M_{NB}	$7.4^{+5.0}_{-1.9}$	1434^{+261}_{-134}	$3.94^{+0.23}_{-0.12}$	$1.45^{+0.06}_{-0.08}$
DUSTY	$M_{M'}$	$9.0^{+4.6}_{-2.5}$	1635^{+309}_{-251}	$4.01^{+0.12}_{-0.15}$	$1.51^{+0.12}_{-0.06}$
DUSTY	T_{eff}	$10.1^{+3.2}_{-1.8}$	n.a.	$4.03^{+0.14}_{-0.08}$	$1.53^{+0.06}_{-0.12}$
DUSTY	$L/L_\odot$	$9.0^{+3.4}_{-1.5}$	1594^{+105}_{-77}	$4.00^{+0.17}_{-0.08}$	$1.50^{+0.04}_{-0.10}$
COND	M_J	$7.9^{+3.8}_{-1.5}$	1490^{+124}_{-93}	$3.96^{+0.20}_{-0.09}$	$1.47^{+0.04}_{-0.11}$
COND	M_H	$8.5^{+3.5}_{-1.4}$	1544^{+107}_{-68}	$3.98^{+0.18}_{-0.08}$	$1.48^{+0.04}_{-0.09}$
COND	M_{K_s}	$9.7^{+3.1}_{-1.3}$	1663^{+84}_{-53}	$4.02^{+0.15}_{-0.07}$	$1.52^{+0.03}_{-0.08}$
COND	$M_{L'}$	$11.7^{+2.6}_{-2.3}$	1838^{+112}_{-131}	$4.06^{+0.10}_{-0.09}$	$1.58^{+0.07}_{-0.08}$
COND	M_{NB}	$9.4^{+3.9}_{-1.1}$	1636^{+178}_{-153}	$4.01^{+0.15}_{-0.11}$	$1.51^{+0.07}_{-0.11}$
COND	$M_{M'}$	$13.2^{+2.0}_{-1.8}$	2017^{+115}_{-131}	$4.07^{+0.01}_{-0.05}$	$1.70^{+0.08}_{-0.08}$
COND	T_{eff}	$10.1^{+3.2}_{-1.8}$	n.a.	$4.03^{+0.14}_{-0.08}$	$1.53^{+0.06}_{-0.12}$
COND	$L/L_\odot$	$9.0^{+3.4}_{-1.5}$	1594^{+105}_{-77}	$4.00^{+0.17}_{-0.08}$	$1.50^{+0.04}_{-0.10}$
FM08/1s	M_J	≥ 7.7	≥ 1333	–	–
FM08/1s	M_H	≥ 10	≥ 1554	–	–
FM08/1s	M_{K_s}	>10	>1400	–	–
FM08/1s	$M_{L'}$	>10	>1400	–	–
FM08/1s	M_{NB}	>10	>1400	–	–
FM08/1s	$M_{M'}$	>10	>1400	–	–
FM08	T_{eff}	≥ 9.0	n.a.	–	–
FM08	$L/L_\odot$	≥ 8.0	≥ 1496	–	–
FM08/5s	M_J	≥ 9.6	≥ 1483	–	–
FM08/5s	M_H	≥ 10	>1554	–	–
FM08/5s	M_{K_s}	>10	>1400	–	–
FM08/5s	$M_{L'}$	>10	>1400	–	–
FM08/5s	M_{NB}	≥ 10	≥ 1400	–	–
FM08/5s	$M_{M'}$	>10	>1400	–	–
SB/cf1s	M_J	$7.4^{+1.0}_{-1.0}$	–	$3.98^{+0.12}_{-0.12}$	$1.41^{+0.1}_{-0.1}$
SB/cf1s	M_H	$9.2^{+0.5}_{-0.5}$	–	$4.06^{+0.09}_{-0.09}$	$1.43^{+0.1}_{-0.1}$
SB/cf1s	$M_{L'}$	≥ 10	–	–	–
SB/cf3s	M_J	$7.8^{+1.0}_{-1.0}$	–	$4.00^{+0.12}_{-0.12}$	$1.42^{+0.1}_{-0.1}$
SB/cf3s	M_H	$9.1^{+0.5}_{-0.5}$	–	$4.06^{+0.09}_{-0.09}$	$1.43^{+0.1}_{-0.1}$
SB/cf3s	$M_{L'}$	≥ 10	–	–	–
SB/hy1s	M_J	≥ 9.5	–	–	–
SB/hy1s	M_H	$9.5^{+0.5}_{-0.5}$	–	$4.07^{+0.09}_{-0.09}$	$1.43^{+0.1}_{-0.1}$
SB/hy1s	T_{eff}	≥ 8.5	n.a.	–	–
SB/hy1s	$L/L_\odot$	≥ 8.2	≥ 1574	–	–
SB/hy1s	$M_{L'}$	≥ 10	–	–	–
SB/hy3s	M_J	≥ 9.9	–	–	–
SB/hy3s	M_H	$9.4^{+0.5}_{-0.5}$	–	$4.08^{+0.09}_{-0.09}$	$1.43^{+0.1}_{-0.1}$
SB/hy3s	$M_{L'}$	≥ 10	–	–	–

Notes. FM08 stands for "Fortney and Marley 2008" models (Marley et al. 2007; Fortney et al. 2008). SB/cf1s, SB/cf3s, SB/hy1s, and SB/hy3s correspond to Spiegel & Burrows (2012) evolutionary models with solar-metallicity cloud-free atmospheres, 3× solar-metallicity cloud-free atmospheres, 1× solar-metallicity cloudy atmospheres, and 3× solar-metallicity cloudy atmospheres, respectively.
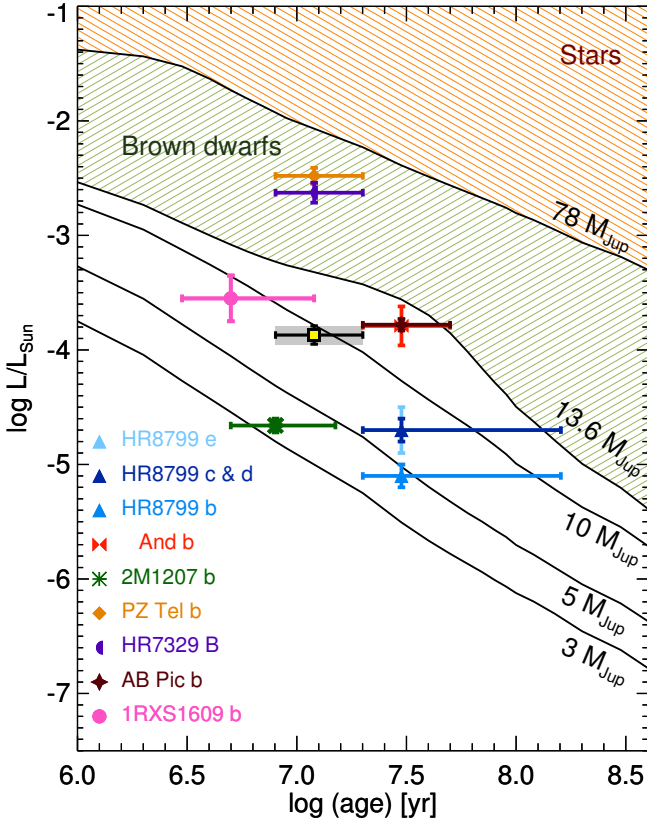
Fig. 9. Luminosities of reference young planetary mass companions compared to COND evolutionary tracks for masses of 3, 5, 10, 13, and 78 M_{Jup}. The luminosities of the two brown-dwarf companions to star members of the β Pictoris moving group (HR 7329 B, PZ Tel b) are overlaid for comparison.

Fig. 10. Luminosity and effective temperatures of β Pictoris b compared to those predicted by "cold-start" (blue curves) and "hot-start" (red curves) models of Fortney et al. (2008) –FM08 – and Spiegel & Burrows (2012) – SB12 – at solar metallicity for different masses and ages.

determined in Sects. 4.1.2 and 4.2. Masses derived from J, H, and M' band photometry agree with those found in previous studies (Lagrange et al. 2010; Bonnefoy et al. 2010; Quanz et al. 2010), with the exeption of COND evolutionary models predictions for the M' band. All predicted surface gravities and radii, but the one derived from the COND evolutionary models in the M' band, are also consistent with those found from the SED fit (see Sect. 4.2). The problem in the M' band could arise from an incorrect representation of the emergent fluxes of β Pictoris b longward 4.0 μm by the associated AMES-Cond atmospheric models. Predictions based on the measured temperature and luminosity should be less affected by this problem. We find masses of $10.1^{+3.2}_{-1.8} M_{Jup}$ and $9.0^{+3.4}_{-1.5} M_{Jup}$ for these two input parameters, respectively. We plot the position of β Pictoris along with those of other young companions in a diagram showing the evolution of the luminosity of objects with planetary, substellar, and stellar masses (Fig. 9). The planet sits above 2M1207b and clearly below the two brown-dwarf companions discovered around stars members of the β Pictoris moving group.

Other "hot-start" models have been proposed by Marley et al. (2007) for 1–10 M_{Jup} planets. Fortney et al. (2008) couple an upgraded version of these models to cloudy atmospheric models with one and five times solar abundances. Models with enriched atmospheres were created to account for the possible enhancement of metal content of exoplanets formed in disks, such as Jupiter and Saturn (see Fortney et al. 2008, and reference therein). We report evolutionary model predictions (generated for the NaCo passbands) for these two choices of boundary conditions in Table 5 and show the location of β Pictoris b
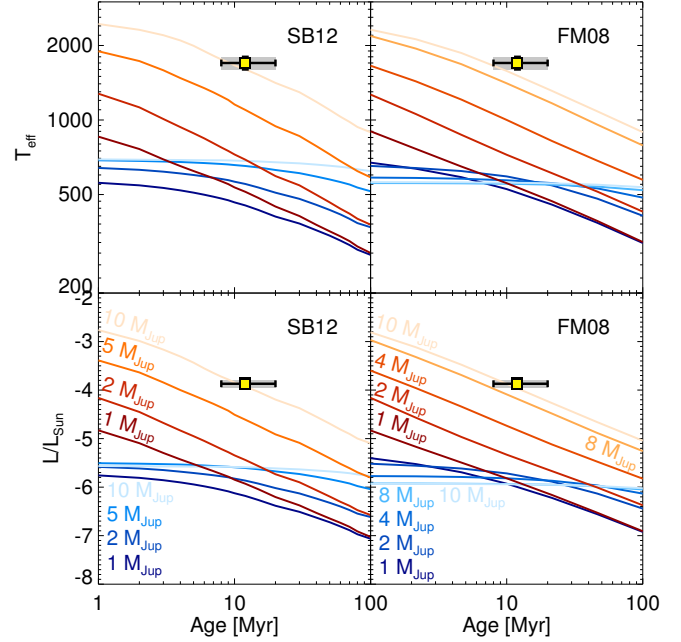
luminosity and T_{eff} with respect to tracks in Fig. 10. Predictions for the highest magnitude values fall above the mass range covered by the model (predictions up to 0.8 mag fainter in the K_s band at solar metallicity, and up to 1 mag fainter in the M' band at five times solar metallicity). For this reason, we are only able to give lower limits on the mass and effective temperature and cannot give secure lower limits for radii and surface gravities. Nevertheless, the lower limits on masses and T_{eff} agree with those derived from DUSTY/COND evolutionary models.

We also use the "hot-start" evolutionary models of Spiegel & Burrows (2012, hereafter SB12) and report predictions in Table 5 for the J, H, and L' band filters. SB12 models consider four atmospheric models (Burrows et al. 2011) as boundary conditions of their interior models: cloud-free models at solar metallicity (hereafter cf1s), three time solar metallicity (cf3s), models with hydrid dust clouds at solar metallicity (hy1s) and models with hydrid clouds with three time solar metallicity (hy3s). We retrieve predictions that agree with estimates from the two other hot-start models. We derived temperature and/or mass predictions from the effective temperature and the luminosity of the planet for the hy1s models[2].

We also compared predictions of the so-called "cold-start" models proposed by Marley et al. (2007) and SB12 to the new β Pictoris b photometry, temperature, and luminosity (see Fig. 10). We confirm that only masses (and lower limits) derived from "hot-start" models agree with the independent upper limit of 15.5 M_{Jup} of the mass of β Pictoris b, given the mass range covered by the models.

---

[2] Predictions come from Fig. 5 and Table 1 of SB12. The temperature for the other boundary conditions are not given in the paper and do not allow a similar comparison.
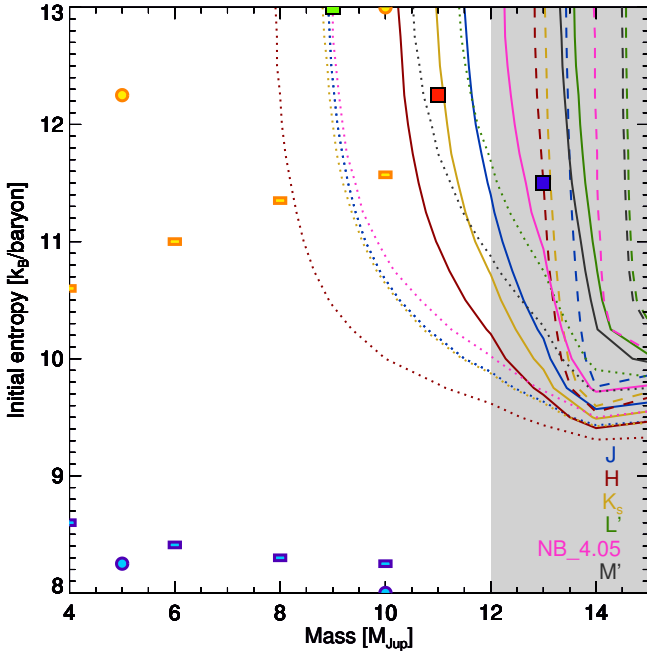
Fig. 11. Masses and initial entropies for β Pictoris b (solid lines) for which warm-start evolutionary models of Spiegel & Burrows (2012) with cloudy atmospheres and solar metallicity (hy1s) at 12 Myr predict the measured absolute magnitudes of the planet. The dotted and dashed lines bracket the range of possible initial entropies and masses of the planet considering the error on the measured photometry and on the age (8–20 Myr) of the system. Green, red, and blue squares correspond to masses and initial entropies for which the predicted photometry simultaneously fit the companion one for ages of 8, 12, and 20 Myr respectively. Masses excluded from current radial velocity measurements and assuming a planetary orbit with a semi-major axis of 9 AU are reported in gray. Yellow and blue dots represent the initial entropies considered in the SB12 hot and cold star models, respectively. Yellow and blue rectangles represent the entropies at 1 Myr in the Marley et al. (2007) hot and cold star models.

4.4.2. "Warm-start" models

Spiegel & Burrows (2012) also propose to explore intermediate cases between cold-start and hot-start models where only a fraction of the gravitational potential energy liberated at the accretion shock do not enter the initial energy budget of the planet. These "warm-start" models do not aim at modeling the formation history self-consistently but instead propose a continuum of evolutionary tracks corresponding to a range of initial entropies ($S_{\rm init}$; from 8 Boltzmann constants per baryon – $k_{\rm B}$/baryon – and up to 13 $k_{\rm B}$; with 0.25$k_{\rm B}$/baryon increments).

We computed the predicted absolute NaCo magnitudes of $1-15\ M_{\rm Jup}$ planets using the predicted "warm-start" low-resolution ($R \sim 200$) spectra[3] of planets placed at 10 pc, the instrument passbands, and the same flux-calibrated spectrum of Vega (Bohlin 2007) used to generate NaCo magnitudes of the LYON tracks. As expected, predicted absolute magnitudes increase with the object mass and $S_{\rm init}$. We report in Fig. 11 the allowed range of $S_{\rm init}$ initial entropies and masses for which β Pictoris photometry matches the prediction of hy3s models for the system age range (12^{+8}_{-20} Myr). This range can be compared to the interval of masses excluded from independent constraints on the mass of the planet.

---

[3] Spectra can be downloaded at http://www.astro.princeton.edu/~burrows/warmstart/spectra.tar.gz

Table 6. Best fitted photometric predictions of the warm-start evolutionary models.

Atmospheric model	Age (Myr)	Mass ($M_{\rm Jup}$)	$S_{\rm init}$ ($k_{\rm B}$/baryon)	χ^2
Cloud free – 1× solar	8	10	11.50	4.64
Cloud free – 3× solar	8	9	13.00	3.40
Hybrid cloud – 1× solar	8	9	13.00	1.59
Hybrid cloud – 3× solar	8	9	12.00	1.59
Cloud free – 1× solar	12	12	11.00	4.86
Cloud free – 3× solar	12	11	13.00	3.49
Hybrid cloud – 1× solar	12	11	12.25	1.67
Hybrid cloud – 3× solar	12	11	11.75	1.69
Cloud free – 1× solar	20	13	13.00	4.94
Cloud free – 3× solar	20	13	11.50	3.62
Hybrid cloud – 1× solar	20	13	11.50	1.75
Hybrid cloud – 3× solar	20	13	11.00	1.76

We also compared our combined set of photometric points to model predictions using a χ^2 minimization (which do not require adjusting a dillution factor). Results of the minimization are reported for 8 Myr, 12 Myr, and 20 Myr predictions and for the four boundary conditions in Table 6. We report the corresponding entropies and masses in Fig. 11.

We reach the following conclusions:

- Single band photometry constrains the planet mass to $\geq 6\ M_{\rm Jup}$. The H-band, L'-band, and M'-band magnitudes of β Pictoris (which tend to be less dependent on the choice of the atmospheric model according to Fig. 8 of SB12) give the same constraints on the initial entropies ($S_{\rm init} \geq 9.3$, 9.6, and 9.7 $k_{\rm B}$/baryon) for the four boundary conditions. The constraints rise to $S_{\rm init} \geq 10.0\ k_{\rm B}$/baryon considering all the bands, the independent mass constraints, and an age of 12 $M_{\rm Jup}$.

- Cloud-free models fail to give coherent predicted masses and initial entropies for the different photometric bands. Cloudy models hy1s and hy3s reduce the dispersion. They predict masses greater than 8 $M_{\rm Jup}$ for the planet and indicate $S_{\rm init} \geq 9.3\ k_{\rm B}$/baryon. Comparatively, cf1s and cf3s models restrain the possible range of initial entropies to $\geq 9.1\ k_{\rm B}$/baryon. If we consider the independent limit of 12 $M_{\rm Jup}$ on the mass of the planet, $S_{\rm init}$ needs to be larger than 9.2 and 9.3 $k_{\rm B}$/baryon for the cf1s and cf3s boundary conditions. The constraint rises to $S_{\rm init} \geq 9.6\ k_{\rm B}$/baryon for hy1s and hy3s atmospheres. These initial entropies all appear greater than those considered for the cold-start models of FM08 and SB12 but lower than those used for the hot-start models. Masses predicted for the lowest magnitude values of the planet at an age of 20 Myr fall in the range proscribed by radial velocity measurements if the planet semi-major axis is 9 AU.

- Results from the combined fit of our photometry confirm the last conclusions. They predict masses between 9 and 13 $M_{\rm Jup}$ and initial entropies ($\geq 11\ k_{\rm B}$/baryon) that correspond better to those of hot-start evolutionary tracks. Masses predicted for a 20 Myr old system fall in the range of masses excluded by dynamical constraints if β Pictoris b semi-major axis is ≤ 9 AU. The χ^2 of the fit is reduced for cloudy atmospheres with solar abundances. This agrees with conclusions derived from atmospheric model fits in Sect. 4.2.

The present analysis suggests that initial conditions lie somewhere between those adopted for cold-start and hot-start models of SB12 and FM08, and more likely lie closer to those adopted

for hot-start models. We discuss the implications of these conclusions in Sect. 5.3.

5. Discussion

5.1. Comparison of the empirical and model-dependent analyses

Comparison of β Pictoris b photometry to empirical objects and atmospheric/evolutionary models converge toward the picture of an exoplanet with a cloudy atmosphere. The effective temperature derived in Sect. 4.2 is compatible with those derived for other young L-type companions, such as AB Pic b ($T_{\mathrm{eff}} = 1700 \pm 100$ K, Bonnefoy et al. 2013b), CD-35 2722 B ($T_{\mathrm{eff}} = 1700-1900$ K, Wahhaj et al. 2011), or 1RXSJ1609-2105b ($T_{\mathrm{eff}} = 1800^{+200}_{-100}$ K, Lafrenière et al. 2008), using similar PHOENIX-based atmospheric models. We also recently derived $T_{\mathrm{eff}} = 1700-1900$ K for a sample of young M9.5-L0 dwarfs comparing their near-infrared spectra to BT-SETTL2010 models (Bonnefoy et al. 2013b). We note, however, some exeptions like the young L0 companion GSC 0621400210 b (Bowler et al. 2011) that has a significant higher estimated temperature ($T_{\mathrm{eff}} = 2700 \pm 200$ K). Nevertheless, we believe that this exeption most certainly arises from the nonhomogeneous classification of these companions[4] and that the present comparison instead validates the self-consistency of the analysis of β Pictoris b near-infrared SED. We also note that the spectroscopic T_{eff} of the planet corresponds to a spectral type in the range L3-L4.5 using the conversion scale of Stephens et al. (2009) valid for field dwarfs. Despite the scale being generated using another family of atmospheric models (e.g. Saumon & Marley 2008), this spectral type range is consistent with the one inferred from the location of β Pictoris with respect to field dwarfs in $J - H$ vs. $H - K_{\mathrm{s}}$ and color–magnitudes diagrams.

If we choose to adopt a spectral type L2$_\gamma$ ± 2 for β Pictoris b, the planet appears to have redder $K_{\mathrm{s}} - L'$ colors than do early-L field dwarfs in Fig. 3. SB12 evolutionary models, and all but the DRIFT-PHOENIX models (Fig. 5) suggest the planet could be overluminous in the L' band. Nonequilibrium chemistry CO $\leftrightarrows$ CH$_4$ induced by the reduced surface gravity of the object might be invoked (Barman et al. 2011b). But BT-Settl (which account for nonequilibrium chemistry) and DRIFT-PHOENIX models predict that the $K_{\mathrm{s}} - L'$ color is mostly independent of the surface gravity of the object. DRIFT-PHOENIX also suggest that metallicity is not able to explain the planet color. The same is true for the other colors represented in Fig. 3. To conclude, one would expect to find a similar location for β Pictoris b and the other young L-type companions in the diagrams. The problem could arise more simply from an error in the neutral density factor estimates. Adopting the default value from the NaCo User Manual (~1.8%; and used for all the studies of β Pictoris b so far) would bring back β Pictoris b colors in better agreement with those of L dwarfs and young companions. But we note that our transmission value relies on three different measurements and are not affected by any residual flux level from background subtraction. The choice of the neutral density transmission does not bias our best-fitted effective temperatures.

---

4 Some of the companions have been classified based on the comparison to mature field-dwarf spectra in the near infrared. A classification scheme that accounts for the different ages of the objects (Kirkpatrick 2005; Cruz et al. 2009) might be more appropriate.

Table 7. Properties of the β Pictoris system.

Parameter	β Pictoris A	β Pictoris b	References
d (pc)	19.44 ± 0.05	–	2
Age (Myr)	12^{+8}_{-4}	–	3
J (mag)	3.524 ± 0.013	14.0 ± 0.3	1, 4
H (mag)	3.491 ± 0.009	13.5 ± 0.2	1, 4
K_{s} (mag)	3.451 ± 0.009	12.6 ± 0.1	4, 5
L' (mag)	3.454 ± 0.003[a]	11.0 ± 0.2	1, 5, 6
NB_4.05 (mag)	–	11.20 ± 0.23	7
M' (mag)	3.458 ± 0.009[a]	11.0 ± 0.3	1, 6
M_J (mag)	2.081 ± 0.014	12.6 ± 0.3	1
M_H (mag)	2.048 ± 0.011	12.0 ± 0.2	1
$M_{K_{\mathrm{s}}}$ (mag)	2.007 ± 0.011	11.2 ± 0.1	5
$M_{L'}$ (mag)	2.011 ± 0.006	9.5 ± 0.2	1, 5
$M_{\mathrm{NB\_4.05}}$ (mag)	–	9.76 ± 0.24	7
$M_{M'}$ (mag)	2.014 ± 0.011	9.5 ± 0.3	1
Spectral type	A6V	L2$_\gamma$ ± 2 :	1, 8
T_{eff} (K)	8052, 8036	1700 ± 100	1, 8, 9
log g (dex)	4.15, 4.21	4.0 ± 0.5	1, 8, 9
M/H (dex)	+0.05, +0.11	0.0 ?	1, 8, 9
$\log_{10} (L/L_\odot)$	0.91 ± 0.01[b]	−3.87 ± 0.08	1
Mass ($M_\odot$)	1.70 ± 0.05[b]	$0.010^{+0.003(c)}_{-0.002}$	1

Notes. [a] ESO L and M-band magnitude. [b] Using the evolutionary tracks of Ekström et al. (2012) with and without rotation. [c] Using COND and DUSTY "hot-start" evolutionary models.

References. (1) – this work; (2) – van Leeuwen (2007); (3) – Zuckerman et al. (2001); (4) – van der Bliek et al. (1996b); (5) – Bonnefoy et al. (2011); (6) – Bouchet et al. (1991); (7) – Quanz et al. (2010); (8) – Gray et al. (2006); (9) – Saffe et al. (2008).

5.2. β Pictoris b abundances

Gray et al. (2006) and Saffe et al. (2008) estimated solar metallicity (M/H = +0.05 and +0.11 respectively) for β Pictoris A by comparing the optical spectra of the star to atmospheric models. The abundances of β Pictoris A are consistent with measurements found for other young nearby association members (Viana Almeida et al. 2009; Biazzo et al. 2012). BT-Settl 2012, DRIFT-PHOENIX, and SB12 models at solar metallicity match the SED of β Pictoris b best. A careful visual check of the fits reveals that differences in magnitudes between the best-fitting SB12 models (and associated χ^2 values) with 1× and 3× solar-metallicities (or M/H = 0 and +0.5 dex respectely) are negligible. The planet would need to be fainter of 0.45 mag in the J band and brighter than 0.25 mag in the K_{s} to be well-fitted by the 3× solar-metallicity DRIFT-PHOENIX models. The J-band of well-fitted metal-enriched BT-Settl2012 models is 1 mag fainter than that of β Pictoris b. The higher departure of BT-Settl2012 models flux in the J band at [M/H] = +0.5 compared to the DRIFT-PHOENIX might come from using different reference solar abundances. The reference solar abundances of Caffau et al. (2011) should tend to make BT-Settl2012 models under-metallic with respect to DRIFT-PHOENIX for the same [M/H] value. Low-resolution spectra of β Pictoris b would now be needed to firmly estimate this atmospheric parameter.

5.3. The formation of β Pictoris b

It is thought that disk instability leads gas to retain much more of its initial entropy than core-accretion, leading to a planet with "hot-start" conditions. New 3D simulations of the collapse of disk clumps confirm this fact (Galvagni et al. 2012).
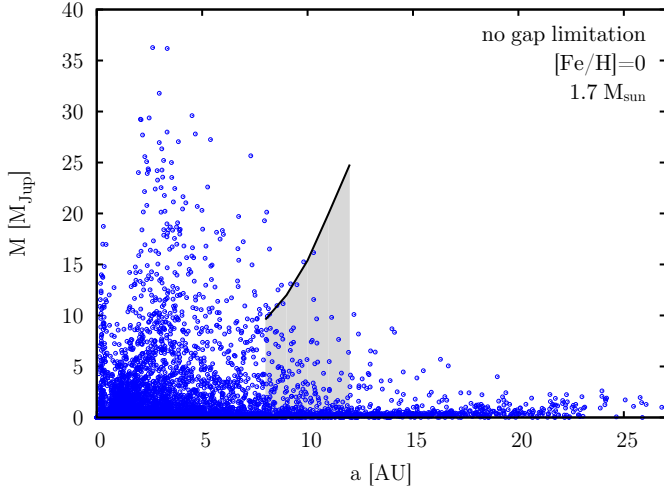
Fig. 12. Population synthesis of planets formed one-by-one by core accretion around a 1.7 $M_\odot$ star. We overlaid limits on the mass coming from radial velocity measurments (black solid line).

Constraints on the initial entropies of β Pictoris b would then suggest a formation by disk instability. Janson et al. (2011) have shown that disk-instability is not the dominant formation scenario of wide-orbit companions around stars more massive than β Pictoris (and then more favorable to disk-instability), using models that can predict within which boundaries in mass/semimajor axis space fragments can form from disk instabilities (see Janson et al. 2011 and Mordasini et al. 2010, for a description of the models). Rameau et al. 2013 (submitted) shows that the same models applied to the case of β Pictoris can only form self-gravitating clumps with masses ≥ 3 $M_{\rm Jup}$ at distances greater than ~ 45 AU from the star. Additional dynamical process, such as tidal interaction with the disk (Baruteau et al. 2011; Michael et al. 2011; Zhu et al. 2012) and/or planet-planet interactions (Boley et al. 2012), would then be needed to explain the present location of the planet.

Nevertheless, Mordasini et al. (2012) argue that the link between cold/hot start evolutionary models and, more generally, the link between initial entropy and the formation scenario (e.g. core-accretion vs. disk instability) cannot presently be established given our limited knowledge of the way the material is accreted, in particular at the accretion shock (Marley et al. 2007; Commerçon et al. 2011). For example, core accretion with a subcritical shock (no radiative losses) also leads to a "hot start". Constraints on the initial entropy could nevertheless be compared to those of planets similar to β Pictoris b (discovered in disks, with dynamical constraints) that will be unearthed by the planet imagers (LBTI/LMIRCam, Subaru/SCExAO, VLT/SPHERE, Gemini/GPI) in coming years.

Could β Pictoris b be formed by core accretion then? Kennedy & Kenyon (2008) suggest that cores can form at $8-10$ AU around a star as massive as β Pictoris. We used here the framework of Mordasini et al. (2012) for planet population synthesis to strengthen this hint. It handles the formation of single planets in disks around solar-mass stars and accounts for disk evolution and migration processes (type I, type II). It can be used to generate population of planets with individual properties that can be compared to the observations. We modified the code in order to simulate the formation of planets around a 1.7 $M_\odot$ star at solar metallicity. The disk mass distribution was shifted by a factor $M_{\rm star}^{1.2}$ with respect to the Mordasini et al. (2012) models in order to get an accretion rate on the star that varies approximately

as $M_{\rm star}^2$ (with $M_{\rm star}$ the stellar mass; see Alibert et al. 2011). We show in Fig. 12 the resulting populations of 50 000 planets.

Synthetic planets as massive as β Pictoris b (considering masses from the hot-start models or dynamical constraints on the mass) can be found at 12 Myr around such a massive star up to ~ 14 AU. Generally, this population synthesis shows that massive planets such as β Pictoris b represent the boundary of the population of planets for the considered semi-major axis. However, we want to stress that these simulations are defined here for a given set of model parameters and that several assumptions have been made. An important assumption in this context is that the gas accretion rate is not reduced due to gap formation (Lubow et al. 1999) because of the eccentric instability (Kley & Dirksen 2006). We did not included disk heating by the irradiation of the host star (viscous heating only) in these simulations. Next, one planet embryo is injected per disk. This situation might not be realistic for β Pictoris given observational clues for additional – but lower mass – planets in the system (e.g. Okamoto et al. 2004). We also took here a core accretion rate of Pollack et al. (1996) that might be too optimistic (Fortier et al. 2013), meaning that we assume that massive cores form relatively quickly. We also assume that massive cores can be formed. In the range of semi-major axis of β Pictoris b ($8-10$ AU), massive planets (>9 $M_{\rm Jup}$) have predicted core masses of 160 to 230 $M_\oplus$. Nevertheless, recent detections of dense transiting companions suggest that this hypothesis is relevant (Deleuil et al. 2008, 2012). Simulations studying the impact on the choice of free parameters (and hypothesis made in the models) and accounting for multiple planets formation per disk would now be needed to better understand the formation of the planet. A forthcoming study (Mollière, in prep.) coupling the formation and evolution (luminosity, $T_{\rm eff}$) of synthetic planets will also lead to a better understanding of whether core-accretion can form high entropy objects at the planet separation.

6. Conclusions

We have presented the first resolved J, H, and M' band images of the exoplanet β Pictoris b. We extracted fluxes of the planet at these wavelengths and combined them to published observations at 2.18, 3.8, and 4.05 μm in order to build the spectral energy distribution of the planet from 1 to 5 μm.

We found that the planet has similar colors and flux to young and old field L0-L4 dwarfs and, in particular, to the ~ 30 Myr old planet/brown-dwarf companion recently discovered around the massive star κ Andromedae. We used these broad spectral type estimates and bollometric corrections defined for young objects to derive $\mathrm{Log}_{10}\,(L/L_\odot) = -3.87 \pm 0.08$ for the planet. Comparison of the planet SED to atmosphere models showed that the atmosphere contains dust and gives a more robust estimate of its effective temperature ($T_{\rm eff} = 1700 \pm 100$ K). Models also suggest that the planet has the reduced surface gravity (log $g = 4.0 \pm 0.5$) characteristic of young objects.

We measured the position of the planet in our new data and combined it with existing astrometry to refine the distribution of orbital parameters. We confirmed that the semi-major axis lies in the 8-10 AU range and the excentricity is lower than or equal to 0.15 (80% probability). This validates the independent upper limit on the mass of the companion of 12 (for an orbit at 9 AU) and 15.5 $M_{\rm Jup}$ (10 AU) derived from radial velocity.

We compared this independent mass determination to predictions of three classes of evolutionary tracks based on different initial conditions. We confirmed that masses predicted

by Marley et al. (2007) and Spiegel & Burrows (2012) "cold-start" evolutionary models for the estimated T_{eff} and photometry of β Pictoris b do not comply with dynamical constraints. Instead, we found that classical "hot-start" models successfully predict the temperature and luminosity of the object for masses of $10^{+3}_{-2}\,M_{Jup}$ and $9^{+3}_{-2}\,M_{Jup}$ respectively. "Warm-start" models, which deal with the intermediate cases between "cold" and "hot-starts", predict masses $\geq 6\,M_{Jup}$. These models also constrain the initial entropy of the planet to $S_{init} \geq 9.3\,k_b/\text{baryon}$. Initial entropy values are then at least midway between those considered for hot-start and cold-start models, and most likely closer to those of hot-start models[5]. We argued that these values cannot presently be used to identify the formation scenario of the planet. We generated a population of planets formed by core accretion around a star as massive as β Pictoris. Some planets of the population have masses and semi-major axis that agree with current estimates for β Pictoris b. We showed in addition that synthetic analogs to β Pictoris b are on the edge of the core-accretion capabilities. A more complete version of these models that is better adapted to the specificities of the β Pictoris system and which explores several free parameters set in the models would now be needed to better understand the formation of the system.

The planet β Pictoris b will likely be used as a reference target for the science verification of the planet imagers SPHERE and GPI next year. These two facilities should pursue the monitoring of the planet orbital motion at a time when it should be close to periastron. The intruments should also easily provide the first low-resolution ($R \lesssim 400$) near-infrared (1–2.5 μm) spectrum of the planet. Spectral features, such as the pseudo-continuum shape from 1.5 to 1.8 μm, will enable a firm confirmation of the intermediate surface gravity of the companion. We could also expect to estimate the metallicity (possibly from the shape of the K-band pseudo-continuum) of the planet.

References

Alibert, Y., Mordasini, C., & Benz, W. 2011, A&A, 526, A63
Allard, F., & Homeier, D. 2012, ArXiv e-prints
Allard, F., Hauschildt, P. H., & Schwenke, D. 2000, ApJ, 540, 1005
Allard, F., Hauschildt, P. H., Alexander, D. R., Tamanai, A., & Schweitzer, A. 2001, ApJ, 556, 357
Allard, F., Guillot, T., Ludwig, H.-G., et al. 2003, in Brown Dwarfs, ed. E. Martín, IAU Symp., 211, 325
Allard, F., Allard, N. F., Homeier, D., et al. 2007, A&A, 474, L21
Allard, F., Homeier, D., & Freytag, B. 2011, in 16th Cambridge Workshop on Cool Stars, Stellar Systems, and the Sun, eds. C. Johns-Krull, M. K. Browning, & A. A. West, ASP Conf. Ser., 448, 91

Allard, F., Homeier, D., & Freytag, B. 2012, Roy. Soc. London Philosoph. Trans. Ser. A, 370, 2765
Allers, K. N., Liu, M. C., Dupuy, T. J., & Cushing, M. C. 2010, ApJ, 715, 561
Augereau, J. C., Nelson, R. P., Lagrange, A. M., Papaloizou, J. C. B., & Mouillet, D. 2001, A&A, 370, 447
Baraffe, I., Chabrier, G., Barman, T. S., Allard, F., & Hauschildt, P. H. 2003, A&A, 402, 701
Barber, R. J., Tennyson, J., Harris, G. J., & Tolchenov, R. N. 2006, MNRAS, 368, 1087
Barman, T. S., Macintosh, B., Konopacky, Q. M., & Marois, C. 2011a, ApJ, 733, 65
Barman, T. S., Macintosh, B., Konopacky, Q. M., & Marois, C. 2011b, ApJ, 735, L39
Baruteau, C., Meru, F., & Paardekooper, S.-J. 2011, MNRAS, 416, 1971
Béjar, V. J. S., Zapatero Osorio, M. R., Pérez-Garrido, A., et al. 2008, ApJ, 673, L185
Beust, H., & Morbidelli, A. 1996, Icarus, 120, 358
Beust, H., & Morbidelli, A. 2000, Icarus, 143, 170
Beust, H., Karmann, C., & Lagrange, A.-M. 2001, A&A, 366, 945
Biazzo, K., D'Orazi, V., Desidera, S., et al. 2012, MNRAS, 427, 2905
Biller, B. A., Liu, M. C., Wahhaj, Z., et al. 2010, ApJ, 720, L82
Boccaletti, A., Chauvin, G., Baudoz, P., & Beuzit, J. 2008, A&A, 482, 939
Boccaletti, A., Augereau, J.-C., Lagrange, A.-M., et al. 2012, A&A, 544, A85
Bohlin, R. C. 2007, in The Future of Photometric, Spectrophotometric and Polarimetric Standardization, ed. C. Sterken, ASP Conf. Ser., 364, 315
Boley, A. C., Payne, M. J., & Ford, E. B. 2012, ApJ, 754, 57
Bonnefoy, M., Chauvin, G., Rojo, P., et al. 2010, A&A, 512, A52
Bonnefoy, M., Lagrange, A.-M., Boccaletti, A., et al. 2011, A&A, 528, L15
Bonnefoy, M., Chauvin, G., & Lagrange, A.-M. 2013a, A&A, accepted
Bonnefoy, M., Currie, T., Marleau, G.-D., et al. 2013b, A&A, submitted
Borysow, A. 2002, A&A, 390, 779
Boss, A. P. 2011, ApJ, 731, 74
Bouchet, P., Schmider, F. X., & Manfroid, J. 1991, AAPS, 91, 409
Bowler, B. P., Liu, M. C., Kraus, A. L., Mann, A. W., & Ireland, M. J. 2011, ApJ, 743, 148
Briceño, C., Luhman, K. L., Hartmann, L., Stauffer, J. R., & Kirkpatrick, J. D. 2002, ApJ, 580, 317
Burgasser, A. J., Geballe, T. R., Leggett, S. K., Kirkpatrick, J. D., & Golimowski, D. A. 2006, ApJ, 637, 1067
Caffau, E., Ludwig, H.-G., Steffen, M., Freytag, B., & Bonifacio, P. 2011, Sol. Phys., 268, 255
Carpenter, J. M. 2001, AJ, 121, 2851
Carson, J., Thalmann, C., Janson, M., et al. 2013, ApJ, 763, L32
Chabrier, G., Baraffe, I., Allard, F., & Hauschildt, P. 2000, ApJ, 542, 464
Chauvin, G., Lagrange, A., Dumas, C., et al. 2004a, A&A, 425, L29
Chauvin, G., Lagrange, A.-M., Dumas, C., et al. 2004b, A&A, 425, L29
Chauvin, G., Lagrange, A.-M., Zuckerman, B., et al. 2005, A&A, 438, L29
Chauvin, G., Lagrange, A.-M., Beust, H., et al. 2012, A&A, 542, A41
Commerçon, B., Audit, E., Chabrier, G., & Chièze, J.-P. 2011, A&A, 530, A13
Cruz, K. L., Kirkpatrick, J. D., & Burgasser, A. J. 2009, AJ, 137, 3345
Currie, T., Burrows, A., Itoh, Y., et al. 2011a, ApJ, 729, 128
Currie, T., Thalmann, C., Matsumura, S., et al. 2011b, ApJ, 736, L33
Currie, T., Fukagawa, M., Thalmann, C., Matsumura, S., & Plavchan, P. 2012, ApJ, 755, L34
Deleuil, M., Deeg, H. J., Alonso, R., et al. 2008, A&A, 491, 889
Deleuil, M., Bonomo, A. S., Ferraz-Mello, S., et al. 2012, A&A, 538, A145
Devillard, N. 1997, The Messenger, 87, 19
Dodson-Robinson, S. E., Veras, D., Ford, E. B., & Beichman, C. A. 2009, ApJ, 707, 79
Ducourant, C., Teixeira, R., Chauvin, G., et al. 2008, A&A, 477, L1
Dulick, M., Bauschlicher, Jr., C. W., Burrows, A., et al. 2003, ApJ, 594, 651
Dupuy, T. J., & Liu, M. C. 2012, ApJS, 201, 19
Ekström, S., Georgy, C., Eggenberger, P., et al. 2012, A&A, 537, A146
Faherty, J. K., Burgasser, A. J., Walter, F. M., et al. 2012, ApJ, 752, 56
Faherty, J. K., Rice, E. L., Cruz, K. L., Mamajek, E. E., & Núñez, A. 2013, AJ, 145, 2
Fortier, A., Alibert, Y., Carron, F., Benz, W., & Dittkrist, K.-M. 2013, A&A, 549, A44
Fortney, J. J., Marley, M. S., Saumon, D., & Lodders, K. 2008, ApJ, 683, 1104
Freytag, B., Allard, F., Ludwig, H.-G., Homeier, D., & Steffen, M. 2010, A&A, 513, A19
Galvagni, M., Hayfield, T., Boley, A., et al. 2012, MNRAS, 427, 1725
Gizis, J. E. 2002, ApJ, 575, 484
Golimowski, D. A., Leggett, S. K., Marley, M. S., et al. 2004, AJ, 127, 3516
Gray, R. O., Corbally, C. J., Garrison, R. F., et al. 2006, AJ, 132, 161
Grevesse, N. 2009, Comm. Asteroseismol., 158, 151
Grevesse, N., Noels, A., & Sauval, A. J. 1993, A&A, 271, 587
Hauschildt, P. H. 1999, NASA STI/Recon Technical Report N, 30685

Hauschildt, P. H., & Baron, E. 1999, J. Comput. Appl. Math., 109, 41
Helling, C., & Woitke, P. 2006, A&A, 455, 325
Helling, C., Ackerman, A., Allard, F., et al. 2008a, MNRAS, 391, 1854
Helling, C., Dehn, M., Woitke, P., & Hauschildt, P. H. 2008b, ApJ, 675, L105
Homeier, D. 2005, Mem. Soc. Astron. It. Supp., 7, 157
Ireland, M. J., Kraus, A., Martinache, F., Law, N., & Hillenbrand, L. A. 2011, ApJ, 726, 113
Janson, M., Bergfors, C., Goto, M., Brandner, W., & Lafrenière, D. 2010, ApJ, 710, L35
Janson, M., Bonavita, M., Klahr, H., et al. 2011, ApJ, 736, 89
Kennedy, G. M., & Kenyon, S. J. 2008, ApJ, 673, 502
Kirkpatrick, J. D. 2005, ARA&A, 43, 195
Kirkpatrick, J. D., Barman, T. S., Burgasser, A. J., et al. 2006, ApJ, 639, 1120
Kley, W., & Dirksen, G. 2006, A&A, 447, 369
Lafrenière, D., Marois, C., Doyon, R., Nadeau, D., & Artigau, É. 2007, ApJ, 660, 770
Lafrenière, D., Jayawardhana, R., & van Kerkwijk, M. H. 2008, ApJ, 689, L153
Lafrenière, D., Jayawardhana, R., & van Kerkwijk, M. H. 2010, ApJ, 719, 497
Lafrenière, D., Jayawardhana, R., Janson, M., et al. 2011, ApJ, 730, 42
Lagrange, A., Gratadour, D., Chauvin, G., et al. 2009, A&A, 493, L21
Lagrange, A., Bonnefoy, M., Chauvin, G., et al. 2010, Science, 329, 57
Lagrange, A.-M., Boccaletti, A., Milli, J., et al. 2012a, A&A, 542, A40
Lagrange, A.-M., De Bondt, K., Meunier, N., et al. 2012b, A&A, 542, A18
Lecavelier Des Etangs, A., & Vidal-Madjar, A. 2009, A&A, 497, 557
Lenzen, R., Hartung, M., Brandner, W., et al. 2003, in SPIE Conf. Ser. 4841, eds. M. Iye, & A. F. M. Moorwood, 944
Looper, D. L., Burgasser, A. J., Kirkpatrick, J. D., & Swift, B. J. 2007, ApJ, 669, L97
Lowrance, P. J., McCarthy, C., Becklin, E. E., et al. 1999, ApJ, 512, L69
Lowrance, P. J., Schneider, G., Kirkpatrick, J. D., et al. 2000, ApJ, 541, 390
Lubow, S. H., Seibert, M., & Artymowicz, P. 1999, ApJ, 526, 1001
Madhusudhan, N., Burrows, A., & Currie, T. 2011, ApJ, 737, 34
Marley, M. S., Fortney, J. J., Hubickyj, O., Bodenheimer, P., & Lissauer, J. J. 2007, ApJ, 655, 541
Marley, M. S., Saumon, D., Cushing, M., et al. 2012, ApJ, 754, 135
Marois, C., Lafrenière, D., Doyon, R., Macintosh, B., & Nadeau, D. 2006, ApJ, 641, 556
Marois, C., Macintosh, B., Barman, T., et al. 2008, Science, 322, 1348
Marois, C., Macintosh, B., & Véran, J.-P. 2010a, in SPIE Conf. Ser., 7736
Marois, C., Zuckerman, B., Konopacky, Q. M., Macintosh, B., & Barman, T. 2010b, Nature, 468, 1080
Mayor, M., & Queloz, D. 1995, Nature, 378, 355
McCaughrean, M. J., & Stauffer, J. R. 1994, AJ, 108, 1382
Michael, S., Durisen, R. H., & Boley, A. C. 2011, ApJ, 737, L42
Milli, J., Mouillet, D., Lagrange, A.-M., et al. 2012, A&A, 545, A111
Mordasini, C., Klahr, H., Alibert, Y., Benz, W., & Dittkrist, K.-M. 2010 [arXiv:1012.5281]
Mordasini, C., Alibert, Y., Klahr, H., & Henning, T. 2012, A&A, 547, A111
Mouillet, D., Larwood, J. D., Papaloizou, J. C. B., & Lagrange, A. M. 1997, MNRAS, 292, 896
Mugrauer, M., Vogt, N., Neuhäuser, R., & Schmidt, T. O. B. 2010, A&A, 523, L1
Neuhäuser, R., Ginski, C., Schmidt, T. O. B., & Mugrauer, M. 2011, MNRAS, 416, 1430
Okamoto, Y. K., Kataza, H., Honda, M., et al. 2004, Nature, 431, 660
Pickles, A. J. 1998, PASP, 110, 863
Plez, B. 1998, A&A, 337, 495
Pollack, J. B., Hubickyj, O., Bodenheimer, P., et al. 1996, Icarus, 124, 62
Quanz, S. P., Meyer, M. R., Kenworthy, M. A., et al. 2010, ApJ, 722, L49
Reid, I. N., Cruz, K. L., Kirkpatrick, J. D., et al. 2008, AJ, 136, 1290
Rice, E. L., Faherty, J. K., & Cruz, K. L. 2010, ApJ, 715, L165
Rossow, W. B. 1978, Icarus, 36, 1
Rousset, G., Lacombe, F., Puget, P., et al. 2003, in SPIE Conf. Ser. 4839, eds. P. L. Wizinowich, & D. Bonaccini, 140
Saffe, C., Gómez, M., Pintado, O., & González, E. 2008, A&A, 490, 297
Saumon, D., & Marley, M. S. 2008, ApJ, 689, 1327
Skemer, A. J., Close, L. M., Szűcs, L., et al. 2011, ApJ, 732, 107
Skemer, A. J., Hinz, P. M., Esposito, S., et al. 2012, ApJ, 753, 14
Smith, B. A., & Terrile, R. J. 1984, Science, 226, 1421
Soummer, R., Pueyo, L., & Larkin, J. 2012, ApJ, 755, L28
Spiegel, D. S., & Burrows, A. 2012, ApJ, 745, 174
Stephens, D. C., Leggett, S. K., Cushing, M. C., et al. 2009, ApJ, 702, 154
Sudol, J. J., & Haghighipour, N. 2012, ApJ, 755, 38
Tanaka, H. K. M. 2005, J. Atmospheric and Solar-Terrestrial Physics, 67, 1544
Testi, L. 2009, A&A, 503, 639
Todorov, K., Luhman, K. L., & McLeod, K. K. 2010, ApJ, 714, L84
van der Bliek, N. S., Manfroid, J., & Bouchet, P. 1996a, AAPS, 119, 547
van der Bliek, N. S., Manfroid, J., & Bouchet, P. 1996b, VizieR Online Data Catalog, J/A+AS/119/547
van Leeuwen, F. 2007, A&A, 474, 653
Viana Almeida, P., Santos, N. C., Melo, C., et al. 2009, A&A, 501, 965
Vigan, A., Langlois, M., Moutou, C., & Dohlen, K. 2008, A&A, 489, 1345
Wahhaj, Z., Liu, M. C., Biller, B. A., et al. 2011, ApJ, 729, 139
Weck, P. F., Schweitzer, A., Stancil, P. C., Hauschildt, P. H., & Kirby, K. 2003, ApJ, 582, 1059
Woitke, P., & Helling, C. 2003, A&A, 399, 297
Woitke, P., & Helling, C. 2004, A&A, 414, 335
Zhu, Z., Hartmann, L., Nelson, R. P., & Gammie, C. F. 2012, ApJ, 746, 110
Zuckerman, B., Song, I., Bessell, M. S., & Webb, R. A. 2001, ApJ, 562, L87
Zuckerman, B., Rhee, J. H., Song, I., & Bessell, M. S. 2011, ApJ, 732, 61

Appendix A: Transmission of neutral density filters

We measured the transmission of the two neutral densities (ND_short, ND_long) installed in NaCo for the J, H, K_s, L', and M' filters using datasets gathered from the ESO archives where bright targets were observed consecutively with and without a neutral density (see Table A.1). Each dataset was reduced with the ESO *Eclipse* package (Devillard 1997). *Eclipse* carried out sky and/or dark subtraction, the division by the flat field, bad pixel flagging, and interpolation. The scripts finally shifted and added dithered images to produce a post-cosmetic frame of the sources. We performed aperture photometry on the sources for each setup and compared them to retrieve the transmission factor (different integration radii were considered depending on the dataset). We repeated the procedure for different targets for given filters to estimate an error on the transmission factor. Values are reported in Table A.2. We considered in addition the transmission factor reported in (Boccaletti et al. 2008) for the ND_short neutral density for the computation of the error in the K_s band. To conclude, we only got a single measurement of the ND_long neutral density transmission in the M' band. We considered a higher error for this transmission based on the impact of the level of fluctuations of the background around the target.

Table A.1. Observations log for the calibration of the neutral density transmission.

Date	Target	Camera	Filter	Neutral density	DIT (s)	NDIT	Nexp	EC Mean (%)	τ_0 mean q (ms)
07/04/2004	HIP 59502	S13	J	ND_short	1.500	25	6	30.8	6.3
07/04/2004	HIP 59502	S13	J	...	0.350	35	6	18.9	3.6
07/04/2004	HIP 61265	S13	J	ND_short	2.500	15	6	39.0	7.0
07/04/2004	HIP 61265	S13	J	...	0.350	35	6	14.9	2.6
09/06/2004	HIP 81949	S13	J	ND_short	2.200	20	6	33.6	4.0
09/06/2004	HIP 81949	S13	J	...	0.350	35	6	29.2	2.7
26/06/2004	HIP 81949	S13	J	ND_short	2.200	20	6	38.7	2.1
26/06/2004	HIP 81949	S13	J	...	0.350	35	6	17.6	1.2
28/11/2005	AB Dor B	S13	J	ND_short	10.000	3	6	35.9	5.3
28/11/2005	AB Dor B	S13	J	...	0.347	100	6	41.1	5.7
09/06/2004	HIP 81949	S13	H	ND_short	2.200	20	6	32.0	3.0
09/06/2004	HIP 81949	S13	H	...	0.350	35	6	28.3	2.5
20/06/2004	GSPC S273-E	S13	H	ND_short	10.000	5	6	22.2	2.4
20/06/2004	GSPC S273-E	S13	H	...	2.000	15	6	13.0	1.5
28/11/2005	AB Dor B	S13	H	ND_short	6.000	2	6	23.6	1.9
28/11/2005	AB Dor B	S13	H	...	0.347	100	6	29.6	2.3
09/06/2004	HIP 81949	S13	K_s	ND_short	5.000	20	6	32.1	3.3
09/06/2004	HIP 81949	S13	K_s	...	0.350	35	6	26.2	1.9
28/11/2005	AB Dor B	S13	K_s	ND_short	2.200	3	6	27.8	3.2
28/11/2005	AB Dor B	S13	K_s	...	0.347	100	6	43.5	4.7
25/12/2009	GSC 08056-00482	L27	L'	ND_long	0.200	100	5	28.9	0.9
25/12/2009	GSC 08056-00482	L27	L'	...	0.200	150	5	42.3	2.9
27/12/2009	WW PsA	L27	L'	ND_long	0.200	100	5	25.3	3.4
27/12/2009	WW PsA	L27	L'	...	0.200	150	5	30.2	12.9
28/12/2009	TX PsA	L27	L'	ND_long	0.200	100	4	36.4	2.0
28/12/2009	TX PsA	L27	L'	...	0.200	150	4	41.8	5.7
03/03/2007	HD158882	L27	M'	ND_long	0.056	70	4	n.a.	n.a.
03/03/2007	HD158882	L27	M'	...	0.056	70	4	n.a.	n.a.

Table A.2. Transmission of the neutral density filters.

Neutral density	Filter	Transmission (%)
ND_short	J	1.42 ± 0.04
ND_short	H	1.23 ± 0.05
ND_short	K_s	1.13 ± 0.04
ND_long	L'	2.21 ± 0.07
ND_long	M'	2.33 ± 0.10

Appendix B: Details on comparison objects

We report in Table B.1 the properties of the young companions and binaries used as comparison objects in Figs. 3 to 5.

Table B.1. Properties of young companions and binaries used as comparison objects.

Name	Distance (pc)	Association	Age (Myr)	Spectral type A	Spectral type b	Separation[a] (AU)	Mass ($M_{\rm Jup}$)	References
HIP 78530B	156.7 ± 13.0	Up. Sco.	5	B9V	M8 ± 1	710 ± 60	22 ± 4	1
GSC 06214-00210b	145 ± 14	Up. Sco.	5	K7	L0 ± 1	320 ± 30	14 ± 2	2, 3
USCO CTIO 108B	145 ± 14	Up. Sco.	5	M7	M9.5	670 ± 64	14^{+2}_{-8}	4
USCO CTIO 108A	145 ± 14	Up. Sco.	5	M7	M9.5	670 ± 64	60 ± 20	4
HR 8799b	39.4 ± 1.0	Columba	30	A5V	L-T	$67.5 - -70.8$	<7	5,6,7,8
HR 8799c	39.4 ± 1.0	Columba	30	A5V	L-T	$42.1 - -44.4$	<10	5,6,7,8
HR 8799d	39.4 ± 1.0	Columba	30	A5V	L-T	$26.4 - -28.1$	<10	5,6,7,8
HR 8799e	39.4 ± 1.0	Columba	30	A5V	L-T	14.5 ± 0.5	<10	6,7,9
2M1207A	52.4 ± 1.1	TW Hydrae	8	M8 pec	$\gtrsim$L5$_\gamma$[b]	40.8 ± 0.9	24 ± 6	10, 11
2M1207b	52.4 ± 1.1	TW Hydrae	8	M8 pec	$\gtrsim$L5$_\gamma$[b]	40.8 ± 0.9	8 ± 2	10,11,12, 13
SDSS J2249+0044A	54 ± 16	Unknown	~100	L3 ± 0.5	L5 ± 1	17 ± 5	29 ± 6	14
SDSS J2249+0044B	54 ± 16	Unknown	~100	L3 ± 0.5	L5 ± 1	17 ± 5	22^{+6}_{-9}	14
AB Pic b	$45.5^{+1.8}_{-1.7}$	Carina	30	K1Ve	L0 ± 1	248 ± 10	$13 - 14$	15, 16, 17
1RXSJ1609-2105b	145 ± 20	Up. Sco.	5	K7V	L4$^{+1}_{-2}$	~330	8^{+4}_{-2}	18, 19
CD-35 2722 B	21.3 ± 1.4	AB Dor	~100	M1Ve	L4 ± 1	67 ± 4	31 ± 8	20
PZ Tel B	51.5 ± 2.6	β Pic	12	K0	M7 ± 2	17.9 ± 0.9	36 ± 6	21, 22
HR 7329 B	47.7 ± 1.5	β Pic	12	A0	M7.5	200 ± 7	26 ± 4	23, 24
TWA 5B	44 ± 4	TW Hydrae	8	M2Ve	M8-M8.5	~98	~20	25
κ Andromedae b	51.6 ± 0.5	Columba	30	B9IV	L2-L8	55 ± 2	12.8^{+2}_{-1}	26

Notes. [a] Projected separations with the exeption of HR 8799bcd where the separations correspond to the latest orbital fit (Currie et al. 2012). [b] Spectral type assumed here given the comparison with the L5$_\gamma$ 2MASS J035523.51+113337.4 (Faherty et al. 2013).

References. (1) – Lafrenière et al. (2011); (2) – Ireland et al. (2011); (3) – Bowler et al. (2011); (4) – Béjar et al. (2008); (5) – Marois et al. (2008); (6) – Zuckerman et al. (2011); (7) – Sudol & Haghighipour (2012); (8) – Currie et al. (2012); (9) – Marois et al. (2010b); (10) – Ducourant et al. (2008); (11) – Gizis (2002); (12) – Chauvin et al. (2004a); (13) – Faherty et al. (2013); (14) – Allers et al. (2010); (15) – Chauvin et al. (2005); (16) – Bonnefoy et al. (2010); (17) – Bonnefoy et al. (2013b); (18) – Lafrenière et al. (2008); (19) – Lafrenière et al. (2010); (20) – Wahhaj et al. (2011); (21) – Biller et al. (2010); (22)– Mugrauer et al. (2010); (23) – Lowrance et al. (2000); (24) – Neuhäuser et al. (2011); (25) – Lowrance et al. (1999); (26) – Carson et al. (2013).